GYROSCOPIC PUMPING IN THE SOLAR NEAR-SURFACE SHEAR LAYER

Mark S. Miesch[1,2] and Bradley W. Hindman[2]

[1]High Altitude Observatory, NCAR[*], Boulder, CO, 80307-3000, USA: miesch@ucar.edu and
[2]JILA and Department of Astrophysical and Planetary Sciences, University of Colorado, Boulder, CO, 80309-0440, USA

Draft version August 30, 2011

ABSTRACT

We use global and local helioseismic inversions to explore the prevailing dynamical balances in the solar Near-Surface Shear Layer (NSSL). The differential rotation and meridional circulation are intimately linked, with a common origin in the turbulent stresses of the upper solar convection zone. The existence and structure of the NSSL cannot be attributed solely to the conservation of angular momentum by solar surface convection, as is often supposed. Rather, the turbulent angular momentum transport accounts for the poleward meridional flow while the often overlooked meridional force balance is required to maintain the mid-latitude rotational shear. We suggest that the base of the NSSL is marked by a transition from baroclinic to turbulent stresses in the meridional plane which suppress Coriolis-induced circulations that would otherwise establish a cylindrical rotation profile. The turbulent angular momentum transport must be non-diffusive and directed radially inward. Inferred mean flows are consistent with the idea that turbulent convection tends to mix angular momentum but only if the mixing efficiency is inhomogeneous and/or anisotropic. The latitudinal and longitudinal components of the estimated turbulent transport are comparable in amplitude and about an order of magnitude larger than the vertical component. We estimate that it requires 2–4% of the solar luminosity to maintain the solar NSSL against the inertia of the mean flow. Most of this energy is associated with the turbulent transport of angular momentum out of the layer, with a spin-down time scale of ∼ 600 days. We also address implications of these results for numerical modeling of the NSSL.

1. INTRODUCTION

Helioseismic inversions of global acoustic oscillation frequencies reveal two striking rotational boundary layers at the upper and lower edges of the solar convective envelope (Thompson et al. 2003; Howe 2009). Throughout the bulk of the convection zone, the angular velocity Ω decreases by about 30% between the equator and latitudes of $\pm 75°$, with conical isosurfaces such that the gradient is primarily latitudinal. Substantial radial gradients in Ω occur only near the base of the convection zone ($0.69R \lesssim r \lesssim 0.72R$, with R as the solar radius) where the super-adiabatic stratification of the envelope meets the sub-adiabatic stratification of the radiative interior, and in the surface layers ($0.95R \lesssim r \lesssim R$) where deep convection meets the heirarchy of smaller-scale convective motions sustained by radiative cooling in the photosphere (Nordlund et al. 2009). The lower boundary layer is known as the solar tachocline and is thought to play an essential role in regulating the dynamical coupling between the convection zone and the radiative interior and in generating the large-scale magnetic fields that underlie the solar activity cycle (Hughes et al. 2007). The upper boundary layer, known as the Near-Surface Shear Layer (NSSL), is similarly complex and enigmatic. Its existence must arise from nonlinear feedbacks among turbulent convective motions spanning vastly disparate spatial and temporal scales with correspondingly different sensitivities to the rotation, density stratification, and spherical geometry.

Although somewhat less celebrated than the

tachocline, the NSSL is more accessible to helioseismic probing and as such, provides a unique window into the dynamics of the solar convection zone. The higher resolution of the helioseismic inversion kernals near the surface allows for a more reliable determination of the rotational gradients. Even more significantly, local helioseismic inversions enable a determination of the meridional flow throughout much of the NSSL to a degree that is not possible in the tachocline. Together with photospheric Doppler and tracer measurements, such inversions indicate a meridional flow that is highly variable but systematically poleward (Snodgrass & Dailey 1996; Hathaway 1996; Haber et al. 2002; Zhao & Kosovichev 2004; González-Hernandez et al. 2006; Ulrich 2010; Basu & Antia 2010; Hathaway & Rightmire 2010, 2011).

Hathaway (2011) has recently suggested that the dynamics that give rise to the poleward meridional flow at the solar surface occur entirely within the NSSL. This conclusion is based on estimates for the subsurface meridional flow obtained from correlation tracking of surface features. These suggest that the poleward surface flow reverses near the base of the NSSL, with equatorward counter-flow at a depth of 35 Mm below the photosphere ($r \approx 0.95R$). This is in contrast to previous estimates based on local helioseismology, which suggest that the poleward flow persists throughout the upper convection zone, with the return flow required by mass conservatation occuring well below 0.95 R (Giles et al. 1997; Giles 1999; Chou & Dai 2001; Beck et al. 2002; Braun & Fan 1998). If confirmed, Hathaway attributes this relatively shallow meridional flow structure to supergranulation.

More specifically, the existence of the NSSL has long been attributed to the tendency for photo-
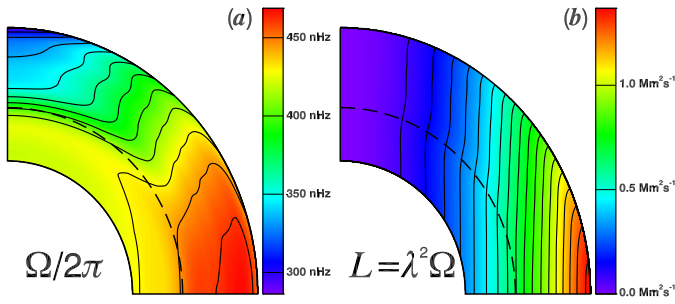
FIG. 1.— (a) Rotation rate Ω and (b) specific angular momentum $\mathcal{L}$ inferred from global helioseismic inversions. Note the sharp decrease in Ω near the surface which defines the NSSL. These results are based on RLS inversions of GONG data from four non-overlapping intervals in 1996, provided by R. Howe (Howe et al. 2000; Schou et al. 2002).

spheric convection (on scales of supergranulation and smaller) to conserve angular momentum locally, with fluid parcels spinning up and spinning down as they move toward and away from the rotation axis respectively (Foukal & Jokipii 1975; Gilman & Foukal 1979; Hathaway 1982; DeRosa et al. 2002; Augustson et al. 2011; Hathaway 2011). Such behavior is often found in numerical simulations of rotating convection when the rotational influence is weak, such that the convective turnover time scale is much less than the rotation period (Gilman 1977; Gilman & Foukal 1979; Hathaway 1982; DeRosa et al. 2002; Aurnou et al. 2007; Augustson et al. 2011). This condition is well satisfied in the solar surface layers where turnover time scales associated with granulation and supergranulation are of order a day or less and the average rotation period is 28 days.

Although the conservation of angular momentum is a valid interpretation of the numerical experiments, it alone cannot account for the existence of the NSSL; there must be more to the story. As we will demonstrate here, meridional forces play an essential role in determining the angular velocity profile in the NSSL, regardless of the nature of the convective angular momentum transport. Furthermore, as we will also demonstrate, the angular velocity profile of the NSSL inferred from helioseismic inversions is not consistent with angular momentum homogenization.

In this paper we propose that the poleward meridional flow in the NSSL is closely linked to the inward Ω gradient. The physical mechanism underlying this link is what we refer to as *gyroscopic pumping*, whereby a zonal forcing (axial torque) induces a meridional flow as a consequence of dynamical equilibration mediated by the inertia of the mean flows (i.e. the Coriolis force). In §2 and §3 we discuss the dynamical balances that are likely to be achieved in the NSSL and in §4 we exploit these dynamical balances in order to estimate the characteristics and efficiency of turbulent transport. Then, in §5 we consider these results from the perspective of two simple theoretical paradigms. We summarize our results and conclusions in §6.

We wish to emphasize from the outset that we are interested in how mean flows, namely differential rotation and meridional circulation, respond to turbulent stresses in the solar NSSL that are currently unknown. Thus, in expressing the relevant dynamical balances we will write

terms involving the inertia of the mean flows (including the Coriolis force) explicitly. Meanwhile, we will incorporate turbulent stresses by means of two relatively generic terms, $\mathcal{F}$ and $\mathcal{G}$, introduced in sections 2.1 and 3.1 (see also Appendix A). The reader who values specificity may regard $\mathcal{F}$ and $\mathcal{G}$ as an embodiment of the convective Reynolds stress, with explicit expressions given in Appendix A. This is likely to be the dominant contribution in the solar NSSL. However, by leaving these terms unspecified we wish to highlight the generality of the physical processes we consider. Thus, the Maxwell stress and the large-scale Lorentz force in stars and the artificial viscous diffusion in numerical simulations can establish mean flows in much the same way.

2. GYROSCOPIC PUMPING

2.1. *Fundamental Concepts*

We begin our investigation of the dynamical balances in the NSSL with the standard (compressible) equations of magnetohydrodynamics (see Appendix A), alternating throughout between spherical polar coordinates (r, θ, ϕ) and cylindrical coordinates (λ, ϕ, z). Thus, $\lambda = r \sin\theta$ is the cylindrical radius and $z = r \cos\theta$ is the coordinate parallel to the rotation axis (each with corresponding unit vectors, e.g. $\hat{\boldsymbol{\lambda}}$).

An equation for the conservation of angular momentum can be readily obtained by multiplying the zonal (ϕ) component of the momentum equation by the moment arm, λ, and then averaging over longitude and time (denoted by angular brackets $<>$). This yields

$$\langle\rho\rangle \frac{\partial \mathcal{L}}{\partial t} = \langle\rho\rangle \lambda^2 \frac{\partial \Omega}{\partial t} = -\langle\rho\mathbf{v}_m\rangle\cdot\boldsymbol{\nabla}\mathcal{L} + \mathcal{F} \quad , \qquad (1)$$

where ρ is the mass density and $\mathbf{v}$ is the bulk velocity, including meridional and zonal components; $\mathbf{v} = \mathbf{v}_m + v_\phi\hat{\boldsymbol{\phi}}$. The term $\mathcal{F}$ incorporates all non-axisymmetric, magnetic, and viscous effects, as described further below and in Appendix A. Thus, we refer to it as the net axial torque. However, if magnetic fields and viscous diffusion are neglected, $\mathcal{F}$ has only one component, and that is the Reynolds stress. We use an inertial (non-rotating) coordinate system so the angular velocity is given by $\Omega = \langle v_\phi\rangle \lambda^{-1}$ and the specific angular momentum is $\mathcal{L} = \lambda^2\Omega$. The meridional velocity can be expressed in spherical and cylindrical coordinates as $\mathbf{v}_m = v_r\hat{\boldsymbol{r}} + v_\theta\hat{\boldsymbol{\theta}} = v_\lambda\hat{\boldsymbol{\lambda}} + v_z\hat{\boldsymbol{z}}$.

If we assume a statistically stationary state equation (1) becomes (e.g. Miesch & Toomre 2009):

$$\langle\rho\mathbf{v}_m\rangle\cdot\boldsymbol{\nabla}\mathcal{L} = \mathcal{F} \quad . \qquad (2)$$

Furthermore, if we assume that there is negligible mass flux through the solar surface, then a steady solution is only possible if

$$\int_V \mathcal{F}dV = 0 \quad , \qquad (3)$$

where V is the volume of the entire solar interior $r \leq R$.

We emphasize that equations (1) and (2) are valid for any arbitrary value of the Rossby number. They follow directly from the MHD equations, as demonstrated in Appendix A. The left-hand-side includes all terms involving the inertia of the mean flow and the right-hand-side. $\mathcal{F}$, is dominated by the Reynolds stress.

More specifically, the left-hand-side of equation (2) repesents the advection of angular momentum by the mean meridional circulation and the right-hand-side incorporates all other forces, most notably the convective Reynolds stress and the Lorentz force. Molecular viscosity can also contribute to the net torque $\mathcal{F}$ but this is expected to be negligible in stars. Any imbalance between the forces that contribute to $\mathcal{F}$ will induce a meridional flow $\langle\rho\mathbf{v}_m\rangle$ across $\mathcal{L}$ isosurfaces. Although Ω contours are nearly radial in the bulk of the solar convection zone, $\mathcal{L}$ contours are nearly cylindrical, as demonstrated in Figure 1, increasing away from the rotation axis such that

$$\boldsymbol{\nabla}\mathcal{L} \approx \frac{\partial\mathcal{L}}{\partial\lambda}\,\hat{\boldsymbol{\lambda}} \qquad (4)$$

and $\partial\mathcal{L}/\partial\lambda > 0$. Thus, equation (2) implies that a retrograde torque $\mathcal{F} < 0$ will induce a flow toward the rotation axis while a prograde torque $\mathcal{F} > 0$ will induce a flow away from the rotation axis. This is the concept of gyroscopic pumping discussed by McIntyre (1998, 2007; see also Haynes et al. 1991, Garaud & Acevedo Arreguin 2009, and Garaud & Bodenheimer 2010). Thus, we refer to equation (2) as the gyroscopic pumping equation.

The process by which equation (2) is established will be addressed in §3. Here we focus on its implications. To proceed, we assume that the mass flux is divergenceless, $\boldsymbol{\nabla}\cdot\langle\rho\mathbf{v}_m\rangle = 0$. This can be justified with the anelastic approximation but that is not necessary; a non-divergent mean mass flux follows directly from the compressible mass continuity equation under the assumption of a statistically stationary state. We may then define a streamfunction Ψ such that

$$\langle\rho v_\lambda\rangle = \frac{\partial\Psi}{\partial z} \quad \text{and} \quad \langle\rho v_z\rangle = -\frac{1}{\lambda}\frac{\partial}{\partial\lambda}\left(\lambda\Psi\right) \quad . \qquad (5)$$

If the $\mathcal{L}$ contours are cylindrical, as expressed in equation (4), then Ψ follows directly from equations (2) and (5):

$$\Psi(\lambda, z) = \left(\frac{d\mathcal{L}}{d\lambda}\right)^{-1}\int_{z_b}^{z}\mathcal{F}(\lambda, z')dz' \qquad (6)$$

where $z_b = (R^2 - \lambda^2)^{1/2}$. In obtaining equation (6) we have assumed that there is no mass flux through the photosphere so $\Psi = 0$ at $r = R$. Thus, Ψ is obtained by integrating along a cylindrical surface, beginning at the photosphere in the northern hemisphere ($z = z_b$) and proceeding in the negative z direction, through the equatorial plane, and continuing to the photospheric boundary in the southern hemisphere ($z = -z_b$).

An appreciation for how gyroscopic pumping operates is best obtained by considering the simplest case in which the differential rotation is weak. This limit is satisfied if $R_o^{DR} << 1$, where $R_o^{DR} = \Delta\Omega/(2\Omega)$ is the Rossby number associated with the differential rotation, and $\Delta\Omega$ is some measure of the variation of the rotation rate with latitude and radius (a rigorous derivation of the limit yields $\Delta\Omega = \lambda\,|\boldsymbol{\nabla}\Omega|$). This criterion is approximately satistied in the Sun; helioseismic inversions indicate $R_o^{DR} \sim 0.16$. In the low Rossby number limit, the uniform rotation component Ω_0 dominates the angular momentum gradient and $d\mathcal{L}/d\lambda = 2\lambda\Omega_0$. Substituting this into (6) then yields Ψ for a given $\mathcal{F}$.

This simple example emphasizes an important point: Here, the net *zonal* force (encompassed in the net axial torque $\mathcal{F}$) determines the *meridional* flow, *not* necessarily the differential rotation. For a given $\mathcal{F}$, equation (2) provides a direct link between the meridional flow and the turbulent angular momentum transport, valid to lowest order in the Rossby number (which is assumed to be small). The differential rotation is determined by other mechanisms, as discussed in §2.2, §3, and §5. An idealized demonstration of how this works is given in Appendix B.

Note also that a cylindrical torque $\mathcal{F} = \mathcal{F}(\lambda)$ is ruled out by equation (6). This would imply a cylindrical mass flux $\langle\rho v_\lambda\rangle$ that is independent of z, which is in turn ruled out by mass conservation and our requirement that there be no flow through the surface $r = R$. More explicitly, we can say that if the $\mathcal{L}$ profile is cylindrical [eq. (4)], then a steady meridional flow is only possible if $\int_{z_b}^{-z_b}\mathcal{F}dz = 0$. In other words, the meridional flow responds mainly to the axial variation of the torque, $d\mathcal{F}/dz$. The amplitude of the resulting $\mathbf{v}_m$ is proportional to $\mathcal{F}$ and inversely proportional to Ω_0; For a given rotation rate, the stronger the zonal force, the stronger the meridional flow that is induced.

For finite values of R_o^{DR} equation (2) must still hold in a steady state but the contribution of the differential rotation to $\boldsymbol{\nabla}\mathcal{L}$ cannot be neglected. The meridional circulation will redistribute angular momentum so $\mathcal{L}$ will depend on Ψ and the gyroscopic pumping equation is nonlinear even if $\mathcal{F}$ is fixed. Linear and nonlinear feedbacks of Ω and Ψ on $\mathcal{F}$ complicate the problem further. A unique solution requires consideration of the meridional momentum and energy equations, as well as mean flow profiles that adjust in order to minimimize the net axial torque $\mathcal{F}$. We address these issues in §2.2 and §3 below.

2.2. *Clarifications and Generalizations*

As emphasized in the last paragraph of §2.1, the gyroscopic pumping equation (2) is robust. It holds for any arbitrary value of the Rossby number provided there exist well-defined, persistent mean flows. Furthermore, $\boldsymbol{\nabla}\mathcal{L}$ is undeniably directed away from the rotation axis in the NSSL, as revealed by global helioseismic inversions (Fig. 1*b*). Thus, the sense and amplitude of the meridional flow is linked to the net axial torque $\mathcal{F}$. However, as also noted in §2.1, this link is in general nonlinear and depends on factors other than the angular momentum transport. In this section we discuss some of the subtleties involved.

We begin with equation (6), which rests on the approximation of a cylindrical angular momentum profile, as expressed in equation (4). Although this is an instructive example with relevance to the Sun (cf. Fig. 1*b*), the concept of gyroscopic pumping is more general and applies straightforwardly to other scenarios as well. In general, the meridional flow through $\mathcal{L}$ isosurfaces is linked to the net axial torque $\mathcal{F}$ while the flow along $\mathcal{L}$ isosurfaces follows from mass conservation. The integral in equation (6) for Ψ would then proceed along $\mathcal{L}$ isosurfaces.

Another issue mentioned in §2.1 concerns the dependence of the net axial torque $\mathcal{F}$ on the mean flows and the possibility that the mean flows adjust to minimize $\mathcal{F}$.

In some circumstances, this dependence may be regarded in terms of a differential operator that operates on the mean rotation profile: $\mathcal{F} = \mathcal{F}\{\Omega\}$. An example is the case of turbulent diffusion, in which the angular momentum flux is proportional to $\boldsymbol{\nabla}\Omega$, as discussed in §5. In this case, the gyroscopic pumping equation (2), admits a homogeneous solution as well as a particular solution. In other words, we may write $\Omega = \Omega_h + \Omega_p$ where

$$\mathcal{F}\{\Omega_h\} = 0 \quad \text{and} \quad \mathcal{F}\{\Omega_p\} = -\langle\rho\mathbf{v}_m\rangle\cdot\boldsymbol{\nabla}\mathcal{L} \quad . \quad (7)$$

This decomposition is only rigorously valid if the operator is linear and if the dependence of the angular momentum advection $\langle\rho\mathbf{v}_m\rangle\mathcal{L}$ on Ω is linearized in some way (e.g. for $R_o^{DR} << 1$). Even so, it serves to illustrate intuitively how the nature of $\mathcal{F}$ has implications for the differential rotation as well as for the meridional circulation. Even in the absence of meridional flow, the solution to the homogeneous equation $\mathcal{F} = 0$ may in general exhibit a differential rotation that depends on the nature of the operator and the boundary conditions. Examples are given in §5.2.

Yet, the basic premise of gyroscopic pumping is still valid, namely that a net axial torque $\mathcal{F} \neq 0$ can only be sustained in a steady state if angular momentum is continually replenished by advection from the surrounding fluid. The meridional flow, differential rotation, and turbulent stresses will adjust until this is achieved. Meridional and zonal forces both play a role in this nonlinear dynamical adjustment as described in §3.2 and contribute to the mean flow profiles that are ultimately realized. Still, the nearly cylindrical $\mathcal{L}$ profile revealed by helioseismology (Fig. 1b) provides a robust link between the meridional flow and the net zonal forcing, expressed in equation (2). Furthermore, the prominent axial Ω gradient $\partial\Omega/\partial z$ revealed by helioseismic inversions provides a robust link between the rotational shear and the meridional forcing, as addressed in §3. Such non-intuitive links between meridional/zonal flows and zonal/meridional forcing are mediated by the Coriolis force so they are most prominent in rapidly rotating systems. However, their robustness applies even in the solar NSSL where the Rossby number based on convection is large (§2.3).

Another important point about gyroscopic pumping is that it is inherently a *non-local* process. A localized torque $\mathcal{F}$ will in general induce a global circulation, extending far beyond the forcing region (Haynes et al. 1991). This has particular significance with regard to the problem of tachocline confinement, whereby gyroscopic pumping in the convection zone induces a circulation that burrows downward into the radiative interior with time unless other physical processes suppress it (Spiegel & Zahn 1992; Gough & McIntyre 1998; Garaud & Brummell 2008; Garaud & Arreguin 2009; Garaud & Bodenheimer 2010). Likewise, zonal forces in the NSSL have potential implications for mean meridional and zonal flows throughout the convection zone. For a demonstration of how a local zonal force in the NSSL can induce a global meridional flow, see the analytic example presented in Appendix B.

Yet, the coupling between the bulk of the convection zone (CZ) and the NSSL will also work the other way. Namely, there must be a net torque in the convection zone $\mathcal{F}_{CZ}$ that induces a meridional flow by gyroscopic pumping that will extend into the NSSL. Furthermore, given the relatively large mass and energy content of the CZ relative to the NSSL, we may expect this meridional flow to overwhelm that which is driven by net axial torques within the NSSL, $\mathcal{F}_{NSSL}$. In order to account for the solar differential rotation, the sense of the deep-seated angular momentum transport must be such that $\mathcal{F}_{CZ}$ is positive at low latitudes and negative at high latitudes. This will induce a counter-clockwise circulation in the northern hemisphere via eq. (2) that will pump mass flux into the NSSL, maintaining a poleward flow even in the absence of any turbulent stresses within the NSSL itself. However, if $\mathcal{F}_{NSSL}$ were indeed zero, then this CZ circulation would redistribute angular momentum until the $\mathcal{L}$ contours aligned with the streamlines of the meridional flow such that $\langle\rho\mathbf{v}_m\rangle\cdot\boldsymbol{\nabla}\mathcal{L} = 0$. This is clearly not the case in the Sun, where the meridional flow is poleward and the $\mathcal{L}$ contours are nearly cylindrical (Fig. 1b). The meridional flow clearly crosses $\mathcal{L}$ isosurfaces, so $\mathcal{F}_{NSSL}$ must be nonzero.

In short, gyroscopic pumping by net axial torques in the deep convection zone may contribute to the poleward flow in the NSSL but angular momentum transport within the NSSL itself must also play a role. This is consistent with the mean-field simulations of Rempel (2005) who considered the maintenance of mean flows in the solar interior based on idealized parameterizations for the turbulent momentum and energy transport. He found poleward meridional flow near the solar surface even without a NSSL. When he included an inward (cf. §5.4) angular momentum transport in a thin layer near the surface, he found both an NSSL-like shear layer where $\partial\Omega/\partial r < 0$ as well as an enhancement of the poleward flow.

2.3. *Implications*

In light of the discussion in §2.1 and §2.2, the implications of equation (2) for the solar NSSL are clear. The same physical mechanism responsible for the deceleration of the rotation rate in the solar surface layers inferred from helioseismology ($\partial\Omega/\partial r < 0$) is also responsible for the poleward meridional flow inferred from helioseismic and Doppler measurements ($\langle v_\theta \rangle < 0$ in the northern hemisphere). The underlying cause of both phenomena is a retrograde net axial torque (zonal force) $\mathcal{F}$ which is most likely due to a divergence in the angular momentum transport by the convective Reynolds stress. Its localization near the solar surface (resulting in a large $\partial\mathcal{F}/\partial z$ that effectively generates a meridional flow) is in turn a likely consequence of the rapidly changing length and time scales of convection, L_c and τ_c. The influence of rotation on convection is typically quantified by the Rossby number based on the convective time scales $R_o = (2\Omega\tau_c)^{-1}$ (as opposed to R_o^{DR} above). Estimates for giant cells ($\tau \sim 10$–20 days, $R_o \sim 0.1$–0.2) and granulation ($\tau \sim 8$ min, $R_o \sim 400$) suggest that R_o should cross unity somewhere in the vicinity of the lower NSSL, likely signifying a qualitative change in convective transport.

Thus, in this section we have established that a net retrograde zonal force $\mathcal{F} < 0$ in the NSSL will induce a poleward meridional flow. This is a very general result, independent of the nature of $\mathcal{F}$, which we address in §5.

Before proceeding to this, however, we discuss another general and important maxim; a net axial torque $\mathcal{F}$ cannot in itself account for the existence of the NSSL. Again, this conclusion is completely independent of the nature of $\mathcal{F}$ and follows essentially from the Taylor-Proudman theorem. Coriolis-induced meridional flows will tend to eliminate all axial rotational shear $\partial\Omega/\partial z$ regardless of the amplitude and structure of the zonal forcing. Thus, the axial shear $\partial\Omega/\partial z$ in the NSSL must be determined not by convective angular momentum transport $\mathcal{F}$ but rather by turbulent and baroclinic stresses in the meridional plane, which we now address (§3).

3. MERIDIONAL FORCE BALANCE

3.1. The Zonal Vorticity Equation

In §2.1 we discussed how a net axial torque $\mathcal{F}$ can induce a meridional circulation through the gyroscopic pumping equation (2) but we said little about how this balance is achieved. We also left open the question of how the differential rotation profile is established, particularly in the low Rossby number limit ($R_o^{DR} << 1$) when $\mathcal{F}$ is directly linked to the meridional flow through eq. (6).

To address these issues for any arbitrary value of the Rossby number, we must also consider the meridional components of the momentum equation. Exploiting the divergenceless nature of the mean mass flux $\langle \rho \mathbf{v}_m \rangle$, we can combine these two equations into one by considering the zonal component of the curl; in other words, the zonal vorticity equation, averaged over longitude and time. In order to illustrate how the system adjusts in response to specified forcing scenarios, we will temporarily retain the time derivative and write this equation as follows:

$$\frac{\partial}{\partial t}\langle \omega_\phi \rangle = \lambda \frac{\partial \Omega^2}{\partial z} + \mathcal{B} + \mathcal{G} \quad , \qquad (8)$$

The vorticity is defined as $\boldsymbol{\omega} = \boldsymbol{\nabla} \times \mathbf{v}$, with ω_ϕ as the zonal component. We emphasize that equation (8) is valid for any arbitrary value of the Rossby number, as demonstrated in Appendix A. The first term on the right-hand side includes the complete inertia of the mean zonal flow, including uniform (Coriolis) and differential rotation components. This is followed by the baroclinic term

$$\mathcal{B} \equiv \frac{\boldsymbol{\nabla}\langle \rho \rangle \times \boldsymbol{\nabla}\langle P \rangle}{\langle \rho \rangle^2} \cdot \hat{\boldsymbol{\phi}} \quad , \qquad (9)$$

where ρ is the density as before and P is the pressure. The final term on the right-hand-side of equation (8), $\mathcal{G}$, represents turbulent stresses in the meridional plane. As with the net axial torque $\mathcal{F}$, $\mathcal{G}$ includes the Reynolds stress, the Lorentz force, and the viscous diffusion. We have also included in $\mathcal{G}$ baroclinic contributions associated with thermal fluctuations, e.g. $\rho' = \rho - \langle \rho \rangle$. An explicit expression for $\mathcal{G}$ is given in Appendix A, along with the derivation of equation (8).

3.2. A Thought Experiment

We now describe a simple thought experiment in order to illustrate several important points about gyroscopic pumping and to gain an intuitive feel for how it operates within the context of the NSSL. We stress that this is an idealized example intended to illustrate fundamental physical principles, namely that some meridional forcing is needed to account for the existence of the NSSL.

We then proceed to discuss the nature of this meridional forcing in §3.3.

Consider a rotating spherical volume of radius R subject to a specified net axial torque $\mathcal{F}$ that turns on at some instant $t = t_0$. In analogy to the NSSL, we will assume that $\mathcal{F} < 0$ in a thin layer near the surface, say $r_s \leq r \leq R$. To be explicit, we can set $r_s \approx 0.95R$ (see §5.2). In order to allow the system to eventually reach an equilibrium state, we assume that the net (integrated) torque in the convection zone is positive, such that $\mathcal{F}$ satisfies equation (3).

For simplicity we will assume that the baroclinic and turbulent stresses in the meridional plane vanish, so $\mathcal{B} = \mathcal{G} = 0$. This corresponds to a flow that is axisymmetric, non-magnetic, non-diffusive, and adiabatic. Furthermore, we assume that $\mathcal{F} = 0$ for $t < t_0$. Thus, before time t_0, the system can sustain an initial equilibrium state with a cylindrical rotation profile $\Omega = \Omega_i(\lambda)$ and no meridional flow, $\mathbf{v}_m = 0$ (satisfying the Taylor-Proudman theorem; see, e.g. Pedlosky 1987). In analogy with the Sun, we assume that the equator rotates faster than the poles, so $d\Omega_i/d\lambda > 0$. It follows also that the angular momentum increases outward, $\boldsymbol{\nabla}\mathcal{L}\cdot\hat{\boldsymbol{\lambda}} > 0$ and is cylindrical ($\boldsymbol{\nabla}\mathcal{L}\cdot\hat{\boldsymbol{z}} = 0$), as expressed in equation (4). This initial equilibrium satisfies equations (2) and (8), with $\partial\langle \omega_\phi \rangle/\partial t = 0$.

Now turn on the torque $\mathcal{F}$ at $t = t_0$. How does the system respond? Initially, the torque will slow down the rotation rate in the NSSL, tilting the Ω contours away from the rotation axis. This will produce an axial rotation gradient $\partial\Omega/\partial z$ which will in turn induce a counter-clockwise meridional circulation in the northern hemisphere (negative $\langle \omega_\phi \rangle$) according to equation (8). In other words, there will be a poleward flow in the NSSL and a net equatorward return flow in the deeper convection zone to ensure mass conservation.

This induced meridional flow will redistribute angular momentum, altering the Ω profile. In the NSSL, angular momentum will be advected from low latitudes toward the poles, accelerating the rotation rate, accompanied by a deceleration of the deeper convection zone. This will proceed until a new, final equilibrium is reached, again with a cylindrical rotation profile $\Omega = \Omega_f(\lambda)$. The new profile will be different from the initial profile ($\Omega_f \neq \Omega_i$), with cylindrical isorotation surfaces shifted away from the rotation axis (positive $\hat{\boldsymbol{\lambda}}$ direction). Furthermore, the torque $\mathcal{F}$ will sustain a steady, nonzero meridional circulation Ψ_f, given by equation (6), with poleward flow in the NSSL and an equatorward return flow in the deep CZ.

In summary, the response of the system to a retrograde zonal torque $\mathcal{F}$ localized in the NSSL is to establish a poleward flow that will increase in amplitude until the prograde angular momentum advected into the layer from the deep CZ balances the retrograde angular momentum imparted by the torque. The meridional flow is predominantly poleward ($\mathbf{v}_m \approx v_\theta\hat{\boldsymbol{\theta}}$) rather than cylindrically inward ($v_\lambda\hat{\boldsymbol{\lambda}}$) because of the thin radial extent of the NSSL (see Appendix B for a demonstration). Meanwhile, the rotation profile is altered but still cylindrical, $\Omega = \Omega_f(\lambda)$.

This simple thought experiment illustrates two important points. First, *gyroscopic pumping is mediated by the*

Coriolis force but the two phenomena are not equivalent.
The meridional components of the Coriolis force can in
principle vanish (for the special case of $\Omega_f = $ constant)
while the system still sustains a gyroscopically-pumped
meridional circulation. More generally, for any cylin-
drical rotation profile $\Omega(\lambda)$, the meridional components
of the Coriolis force are opposed by pressure gradients
(geostrophic balance) so they impart no zonal vorticity
and thus no meridional momentum. The meridional flow
is determined not by the Coriolis force (which responds
to Ω), but rather by the conservation of angular momen-
tum (which responds to $\mathcal{F}$).

The second point is even more important: *The mere
existence of a retrograde torque $\mathcal{F}$ does not guarantee
the presence of a near-surface shear layer.* As stated
in the introduction, even if the concept is valid, angular
momentum conservation by turbulent convection alone
cannot account for the existence of the NSSL. In the
absence of baroclinic, turbulent, or magnetic stresses in
the meridional plane ($\mathcal{B} = \mathcal{G} = 0$), the meridional circu-
lation will wipe out all axial shear $\partial\Omega/\partial z$, *regardless of
the nature, magnitude or profile of the convective angular
momentum transport* (embodied by $\mathcal{F}$).

The robustness of cylindrical rotation profiles is a con-
sequence of the Taylor-Proudman theorem (e.g. Pedlosky
1987). No matter how strong $\mathcal{F}$ is, a commensurate
meridional circulation will suppress axial shear on a time
scale comparable to the rotation period (~ 28 days).
The prominent axial shear $\partial\Omega/\partial z$ exhibited by helioseis-
mic rotation inversions (Fig. 1a) then implies that some
meridional forcing, either baroclinic or "turbulent", $\mathcal{B}$ or
$\mathcal{G}$, is necessary to account for the existence of the NSSL
as well as the detailed structure of the inferred Ω profile.

3.3. *What Determines the Rotational Shear in the NSSL?*

In this section we argue that the existence and location
of the NSSL can be attributed to a qualitative change in
the meridional force balance, marked by a transition from
baroclinic to turbulent stresses; $\mathcal{B}$ to $\mathcal{G}$. Furthermore,
it is the meridional stresses ($\mathcal{G}$ and/or $\mathcal{B}$) rather than
the angular momentum transport that largely determine
the slope of the Ω profile (although the negative sign of
$\partial\Omega/\partial r$ still requires a retrograde net axial torque $\mathcal{F} < 0$).

Although there are still some subtle uncertainties re-
garding the underying dynamics, recent global solar con-
vection simulations and mean-field models have con-
verged on a consistent paradigm whereby the nearly ra-
dial angular velocity contours (conical Ω isosurfaces) at
mid-latitudes in the deep CZ are attributed to baroclinic
forcing

$$\frac{\partial\Omega^2}{\partial z} = -\frac{\mathcal{B}}{\lambda} \approx \frac{g}{r\lambda C_P}\frac{\partial\langle S\rangle}{\partial\theta} \qquad \text{(deep CZ)} \quad (10)$$

where g is the gravitational acceleration, S is the specific
entropy, and C_P is the specific heat at constant pres-
sure (Kitchatinov & Rüdiger 1995; Elliott et al. 2000;
Robinson & Chan 2001; Brun & Toomre 2002; Rempel
2005; Miesch et al. 2006; Brun et al. 2011). This is
referred to as thermal wind balance (Pedlosky 1987;
Miesch & Toomre 2009). The convective Reynolds stress
is still necessary to account for the amplitude and
sense of the angular velocity contrast between equator

and pole, $\Delta\Omega$, but without baroclinicity, models gen-
erally yield cylindrical (Taylor-Proudman) profiles, in
contrast to the conical profiles inferred from helioseis-
mic inversions (Fig. 1a). In early models, the latitudi-
nal entropy gradient in equation (10) is established en-
tirely by a latitude-dependent convective heat flux at-
tributed to the influence of rotation on convective mo-
tions (Kitchatinov & Rüdiger 1995; Elliott et al. 2000;
Robinson & Chan 2001; Brun & Toomre 2002). How-
ever, recent models have demonstrated that thermal cou-
pling to the subadiabatic portion of the tachocline by
means of a gyroscopically-pumped meridional circula-
tion may contribute to establishing the requisite thermal
gradients (Rempel 2005; Miesch et al. 2006; Brun et al.
2011).

In any case, the nature and prominence of the baro-
clinic term in convection simulations and mean-field
models hinges on the low effective Rossby number in the
deep CZ. By *effective* Rossby number we are referring to
the amplitude of the meridional components of the con-
vective Reynolds stress relative to the deflection of the
differential rotation by the Coriolis force and the baro-
clinic forcing. However, as noted in §2.3, the Rossby
number rises steadily with radius in the convection zone,
becoming much greater than unity in the NSSL. This
alone suggests that the turbulent stresses, represented
by $\mathcal{G}$, may overwhelm the baroclinic term $\mathcal{B}$ in the solar
surface layers. *In fact, this shift in the meridional force
balance (from $\mathcal{B}$ to $\mathcal{G}$) may mark the base of the NSSL
even more significantly than a change in the turbulent
angular momentum transport $\mathcal{F}$.*

Thus, we propose that in the NSSL thermal wind bal-
ance, equation (10) is replaced by

$$\frac{\partial\Omega^2}{\partial z} = -\frac{\mathcal{G}}{\lambda} \qquad \text{(NSSL)}. \qquad (11)$$

The implication would then be that *turbulent stresses
in the meridional plane, $\mathcal{G}$, largely determine the dif-
ferential rotation profile in the NSSL.* This hypothesis
is consistent with global simulations of solar convection
which, although they do not yet reproduce the NSSL,
do exhibit a departure from thermal wind balance in
the surface layers above $r \sim 0.95$ (Elliott et al. 2000;
Brun et al. 2010, 2011). This departure is attributed to
a combination of resolved convective Reynolds stresses
and modeled sub-grid scale diffusion, both captured in
our turbulent transport term $\mathcal{G}$. Achieving a NSSL in
global convection simulations will likely require a reli-
able representation of turbulent transport by unresolved
(subgrid-scale) motions, as discussed in §2 and §5.

Can solar observations and models reveal what the
meridional force balance is in the NSSL, or in other
words, which is bigger, $\mathcal{B}$ or $\mathcal{G}$? In principle the answer
is yes, but as we discuss in the remainder of this section,
current results are inconclusive.

Helioseismic rotational inversions provide a good es-
timate for the left-hand-side of equation (10), namely
$\mathcal{C} = -\lambda\partial\Omega^2/\partial z$ (§4). If we had a reliable estimate for
the right-hand-side, $\mathcal{B}$, from solar observations and if its
amplitude were $<< \mathcal{C}$, then we could rule out equation
(10) and thereby verify the proposed balance expressed
in equation (11).

One way to estimate the amplitude of $\mathcal{B}$, at least in

principle, is by means of helioseismic structure inversions. The thermal gradients that give rise to $\mathcal{B}$ imply aspherical sound speed variations. If these gradients are to balance the axial shear in the rotation rate through baroclinic torques as expressed in equation (10), then their relative amplitude must be of order

$$\frac{\Delta S}{C_p} \sim \frac{2}{\pi C_P} \frac{\partial \langle S \rangle}{\partial \theta} \sim \frac{2r\lambda}{\pi g} \frac{\partial \Omega^2}{\partial z} \sim 2 \times 10^{-5} \qquad (12)$$

where ΔS is the entropy variation from equator to pole. The numerical estimate in equation (13) is based on global rotational inversions as described in §4 below.

Such subtle thermal variations are beyond the detection limit of current helioseismic structure inversions, even in the NSSL (Gough et al. 1996; Christensen-Dalsgaard 2002). Brun et al. (2010) have reported aspherical sound speed variations much larger than this, of order 10^{-5}–10^{-4}, but the amplitude of the variations peaks near the base of the convection zone at high latitudes, where the reliability of the inversions is questionable. If these inversions are indeed valid and if they do indeed trace thermal gradients as opposed to magnetic effects, then thermal wind balance, equation (10) would not be satisfied and turbulent stresses $\mathcal{G}$ would have to contribute to the meridional force balance throughout the deep convection zone as well as the NSSL. More work is needed to set stricter limits on aspherical sound speed variations from helioseismic structure inversions and whether they are consistent with helioseismic rotational inversions within the context of thermal wind balance. For now we regard the issue as not yet settled.

An independent estimate for $\mathcal{B}$ near the solar surface can (again, in principle) be obtained from photospheric irradiance measurements. The final equality in equation (10), expressing $\mathcal{B}$ in terms of the latitudinal entropy gradient, applies for an ideal gas equation of state and a nearly hydrostatic, adiabatic stratification (e.g. Miesch & Toomre 2009). An alternative expression can be obtained by assuming that the photosphere is an isobaric surface. In this case the baroclinic term can be expressed in terms of the photospheric temperature variation from equator to pole, ΔT. If this is to balance the Coriolis term $\mathcal{C}$, then we must have relative temperature variations of the same order as in equation (12):

$$\frac{\Delta T}{T} \sim \frac{2}{\pi} \frac{\partial}{\partial \theta} \ln \langle T \rangle \sim \frac{2R\lambda}{\pi g} \frac{\partial \Omega^2}{\partial z} \sim 2 \times 10^{-5} \quad . \qquad (13)$$

We have again assumed an ideal gas equation of state and hydrostatic balance for simplicity. If we further assume that the solar irradiance arises from blackbody emission, then we should expect to see a corresponding latitudinal variation of the irradiance. In other words, if the solar differential rotation in the NSSL were indeed in thermal wind balance [eq. (10)], then we would expect the poles to be brighter than the equator with a relative irradiance enhancement of $\Delta I/I \sim 8 \times 10^{-4}$. This corresponds to a temperature difference of about 0.1K.

Irradiance variations of at least this order have indeed been detected (reviewed by Rast et al. 2008). In particular, recent measurments by Rast et al. (2008) indicate that the poles are indeed brighter than the equator, with $\Delta I/I \sim 1.5 \times 10^{-3}$. However, whether or not these can be interpreted as temperature variations is questionable.

There is a strong possibility that the irradiance variation arises instead from unresolved magnetic flux elements. Thus, we view current estimates of $\mathcal{B}$ based on photospheric irradiance measurements as inconclusive as well.

The essential question is whether $\mathcal{B}$ can keep up with the sharp increase in $\partial \Omega/\partial z$ throughout the NSSL. The answer depends on the details of convective heat transport in the solar surface layers, which are not well understood. If convection acts as a turbulent thermal diffusion, then the thin shell geometry implies that the latitudinal temperature gradient (ΔT) at the base of the NSSL, $r = r_s$, might be efficiently transmitted to the surface. The rapid decrease of the background temperature with radius might then lead to an enhancement of the relative latitudinal temperature gradient $\Delta T/T$, which in turn would imply an increase in $\mathcal{B}$ [cf. eq. (13)]. However, the horizontal heat transport and poleward meridional flow would tend to suppress latitudinal thermal gradients (ΔT) and thus diminish $\mathcal{B}$.

To approach this issue more quantitatively, we estimate from helioseisimic inversions (§4) that $\mathcal{C}$ is a factor of 5-10 larger at the surface than at the base of the NSSL, $r = r_s \sim 0.946R$ (defined as where the mean radial Ω gradient changes sign; see §5.2). Over that same radial range the background temperature decreases by a factor of 30-40. Thus, taking into account also the variation of g and r, we estimate that horizontal transport would have to be at least three times more efficient than vertical transport in order for the magnitude of $\mathcal{B}$ to increase less rapidly than $\mathcal{C}$, assuming thermal wind balance at $r = r_s$ and that the photosphere is an isobaric surface, as in equation (13). We may expect the ratio of horizontal to vertical turbulent diffusion to scale as $\kappa_h/\kappa_v \sim U_h L_h/(U_v L_v)$ where U and L are typical velocity and length scales and h and v denote horizonal and vertical directions. Mass conservation, $\nabla \cdot (\rho \mathbf{v}) = 0$ implies $U_h/U_v \sim L_h/L_v$, so $\kappa_h/\kappa_v \sim (L_h/L_v)^2$. It is reasonable to expect that this ratio may indeed exceed three for solar surface convection. For example, if we put in numbers for granulation, $L_h \sim 1$ Mm and $L_v \sim H_\rho \sim 300$ km, where H_ρ is the density scale height, then $\kappa_h/\kappa_v \sim 10$. This helps to substantiate the conjecture that baroclinic forces may be too weak to balance the Coriolis force associated with the differential rotation in the NSSL.

In summary, we suggest that the characteristic change in the slope of the Ω profile that defines the NSSL is largely determined by a shift in the meridional force balance from baroclinic to turbulent stresses; that is, from equation (10) to equation (11). Although this hypothesis is in principle testable, we believe that current data is insufficient to either confirm or deny it. In the remainder of this paper we assume that this transition does indeed occur and we explore its implications with regard to the dynamics of the NSSL.

Note also that the statements made in this section apply mainly to the persistent, background component of the mean flow that is present throughout the solar cycle. The baroclinic term $\mathcal{B}$ may well establish time-varying meridional and zonal flows such as the low-latitude branch of the solar torsional oscillation as discussed by Spruit (2003) and Rempel (2007). In the Spruit-Rempel model, enhanced cooling in magnetically active latitudinal bands induces converging meridional

flows that in turn accelerate zonal flows by means of the Coriolis force. If the cooling is sustained for at least several months (long enough for the Coriolis force to fully respond), then the dynamical balances in equation (2) and (10) can be established in a quasi-static sense. As for the persistent background flow, the coupled inertia of the fluctuating flow components provides a tight link between the meridional circulation and the rotational shear.

4. HELIOSEISMIC ESTIMATES OF TURBULENT TRANSPORT

In §2 and §3 we argued that the dynamical balances that are likely to prevail in the NSSL are given by equations (2) and (11). The left-hand side of each of these equations involves quantities that are accessible to helioseismic inversions, namely Ω and $\langle \mathbf{v}_m \rangle$. Thus, if we assume these balances hold, then we can obtain observational estimates for the turbulent stresses $\mathcal{F}$ and $\mathcal{G}$.

That is the focus of this section. We will obtain estimates for the turbulent stresses $\mathcal{F}$ and $\mathcal{G}$ based on local and global helioseismic inversions and we will discuss their implications for the nature of turbulent transport in the NSSL. Then, in §5 we will investigate whether these results are consistent with simple theoretical models. We begin in §4.1 by discussing the data we use and we then proceed to calculate $\mathcal{F}$ and $\mathcal{G}$ in §4.2.

4.1. Helioseismic Data and Inversions

We use both local and global helioseismic procedures to estimate the solar rotation rate Ω and the meridional flow component $\langle \mathbf{v}_m \rangle$. Both techniques exploit the fact that, through the Doppler effect, a flow induces a frequency splitting between acoustic waves propagating in opposite directions. By measuring this frequency splitting for a variety of waves that reside within different regions of the solar interior, through an inversion process, maps of the flow as a function of latitude and depth can be produced. Global helioseismology employs modes of long horizontal wavelength that comprise the sun's global acoustic resonances. The frequency splittings of such modes can be used to measure the axisymmetric component of the rotation rate over a broad range of latitudes (within 70° of the equator) and to depths spanning the entire convection zone. Local helioseismic techniques, which measure short-wavelength waves, do not permit sampling of the flows to such high latitudes or to such large depths (only within 50° of the equator and only within the upper 15 Mm or 2% by fractional radius); however, local helioseismology is capable of measuring both the rotation rate and the meridional component of the flow, unlike global helioseismology.

We utilize a local helioseismic procedure called ring analysis which assesses the speed and direction of subsurface horizontal flows by measuring the advection of ambient acoustic waves by those flows (e.g. Hill 1988; Haber et al. 2002). Measurement of the frequency splitting provides a direct measure of the fluid's flow velocity in those layers where the waves have significant amplitude. The frequency shift induced by the flow on any given wave component is given by $\Delta \omega = \mathbf{k} \cdot \bar{\mathbf{U}}$, where $\mathbf{k}$ is the wave's horizontal wavenumber and $\bar{\mathbf{U}}$ is the integral over depth of the horizontal flow velocity weighted by a kernel which is approximately the kinetic energy density of the acoustic wave. The frequency splittings for a
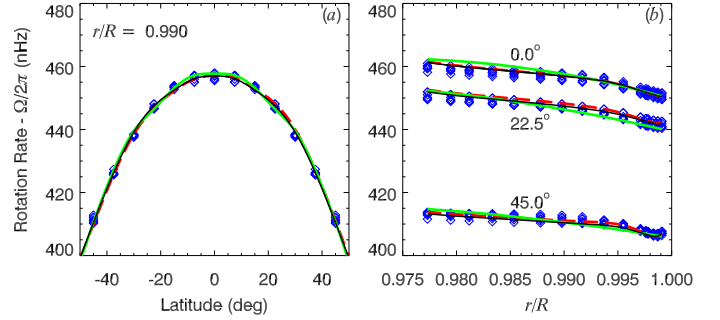

FIG. 2.— Rotation profile Ω obtained from local and global inversions, plotted verses (a) latitude (at the indicated radius) and (b) radius (at the indicated latitudes). Inversions for the year 1996 are shown as a black line and other years 1997-2003 are shown as blue symbols. The green curve represents the global rotation inversions shown in Figure 1 and the dashed red curve represents an analytic fit to the local 1996 inversions of the form expressed in equation (16) below.
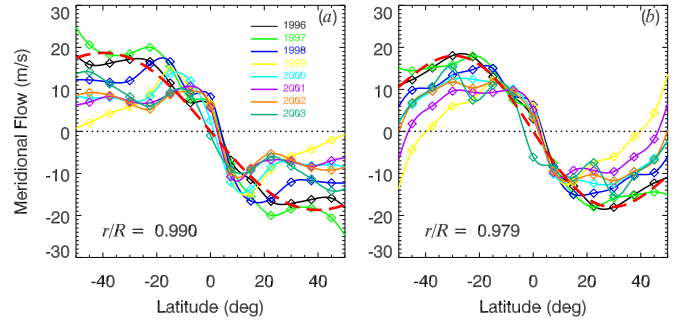

FIG. 3.— Longitudinally-averaged (co-) latitudinal velocity $\langle v_\theta \rangle$ obtained from local helioseismic inversions (ring analysis), plotted versus latitude at (a) $r = 0.990R$ and (b) $r = 0.979R$. Black lines and symbols denote data from 1996 and other colors denote other years, as indicated. We focus on 1996 but we show other years merely to highlight the magnitude of the variations; the relationship between meridional flow variations and solar activity has been investigated in detail elsewhere (e.g. Hathaway 1996; Haber et al. 2002; Zhao & Kosovichev 2004; González-Hernandez et al. 2006; Ulrich 2010; Hathaway & Rightmire 2010, 2011). The red dashed lines represent a fit to the 1996 inversions as expressed in equation (17).

large number of waves of different wavenumber and radial mode order form a system of integral equations that can be inverted to obtain the horizontal flow as a function of depth (Thompson et al. 1996; Haber et al. 2004). By repeating the analysis over many different locations on the solar surface and over many different days, a map of the horizontal flow as a function of longitude, latitude, depth and time can be generated.

Our local helioseismic inferences were made using Dopplergram data from the Michelson Doppler Imager (MDI) aboard the Solar and Heliospheric Observer (SoHO). Flows have been obtained using the Dynamics Campaign data, of which 2-3 months of data per year is available. We have chosen to use data from the rising phase of the solar cycle from 1996 through 2003. The short-wavelength waves used by local helioseismic procedures are trapped near the solar surface, and the ring-analysis measurements used here are therefore capable of sampling down to a depth of 15 Mm below the photosphere, or the upper half of the NSSL. Each local analysis samples a region of Sun that is roughly 180 Mm (15° in

heliographic angle) in diameter. On any given day, a mosaic of 189 overlapping analysis regions are independently analyzed, resulting in a flow map with a horizontal spacing of 7.5° between measurement regions, each with a horizontal resolution of 15°.

Estimates for the mean rotation rate Ω and the latitudinal component of the meridional flow $\langle v_\theta \rangle$, have been obtained by averaging the resultant maps over all longitudes and over the 2-3 months that the Dynamics Campaign data is available each year. The mean rotation rate Ω is illustrated in Figure 2. The black curve corresponds to measurements made in 1996, while the blue diamonds show the weak variability in the flows during the years 1997 to 2003. The latitudinal component of the flow, $\langle v_\theta \rangle$, is shown in Figure 3 at two different depths and with a differently-colored curve for each year.

The global helioseismic assessments were made using four non-overlapping 60 day intervals of GONG data from the year 1996 (Howe et al. 2000; Schou et al. 2002). The rotation rate is inferred from the frequency splitting between modes of equal but opposite azimuthal order $\pm m$. Such modes are identical in all respects other than the fact that they propagate in opposite directions in longitude around the sun. Solar rotation Doppler shifts the mode frequencies in opposite directions and the frequency splittings of many different modes can be inverted to obtain the rotation rate as a function of latitude and depth. The result of a regularized Least Squares (RLS) inversion is shown in Figures 1 and 2.

4.2. Estimating $\mathcal{F}$ and $\mathcal{G}$

If we assume the dynamical balances in equations (2) and (11) hold, then we can turn them around and calculate $\mathcal{F}$ and $\mathcal{G}$ based on helioseismic inversions. In particular, if we assume that to lowest order $\rho \approx \langle \rho \rangle$, then equation (2) yields an estimate of the specific torque

$$\mathcal{T} = \frac{\mathcal{F}}{\rho} = \langle \mathbf{v}_m \rangle \cdot \boldsymbol{\nabla} \mathcal{L} = \langle v_r \rangle \frac{\partial \mathcal{L}}{\partial r} + \frac{\langle v_\theta \rangle}{r} \frac{\partial \mathcal{L}}{\partial \theta} \quad . \quad (14)$$

Thus, the right-hand-side only depends on $\mathcal{L} = \lambda \langle v_\phi \rangle = \lambda^2 \Omega$ and $\langle \mathbf{v}_m \rangle$. Similarly, equation (11) gives

$$\mathcal{G} = -\lambda \frac{\partial \Omega^2}{\partial z} \quad (15)$$

which only depends on Ω.

Estimates for $\mathcal{F}$ and $\mathcal{G}$ based on equations (14) and (15) are shown in Figure 4. In the remainder of this section we provide further details on how these results were obtained. For both $\mathcal{F}$ and $\mathcal{G}$ we focus on data from 1996. Since this corresponds to solar minimum, it minimizes the influence of the cyclic component of the solar magnetic field, focusing instead on the persistent turbulent stresses that maintain the NSSL throughout the solar cycle (§4.4).

Before proceeding to the more involved calculation of $\mathcal{F}$, we first consider the estimate for $\mathcal{G}$ shown in Figure 4b. Since this only depends on Ω, we use the global inversions shown in Figure 1 to compute it. These extend to higher latitudes and lower radii than the local inversions and the longitudinal coverage provided by global modes may more accurately reflect the axisymmetric Ω gradients in the NSSL. In order to compute the latitudinal Ω gradient,
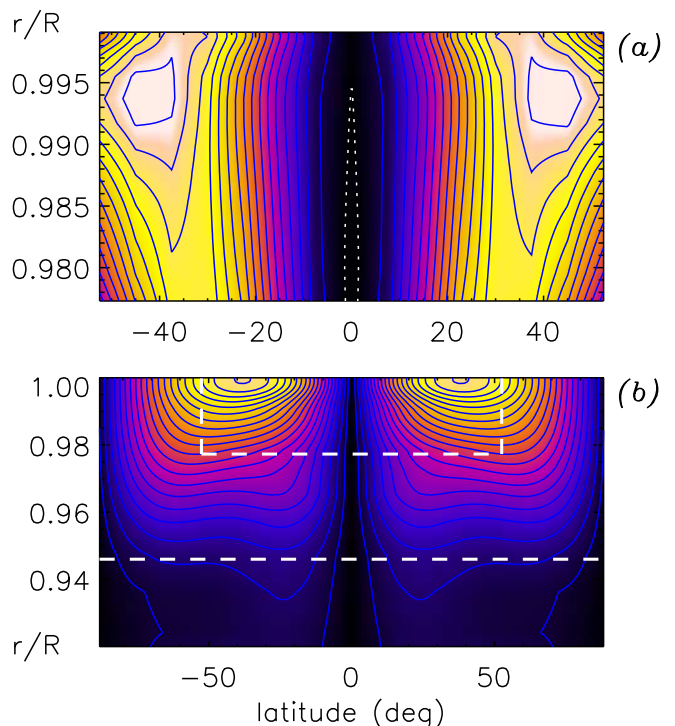
FIG. 4.— Estimates for the turbulent stresses (a) $\mathcal{T} = \mathcal{F}\rho^{-1}$ and (b) $\mathcal{G}$, computed from equations (14) and (15) using local and global helioseismic inversions from 1996, as described in the text. In (a), the color table ranges from -3.95×10^8 cm^2 s^{-1} (white) to zero (black). Blue contours denote negative values and the white dotted line indicates the zero contour. In (b) the color scale runs from zero (black) to 1.28×10^{-11} s^{-2}, with blue contours denoting positive values. Note that the vertical and horizontal axes are different in frames (a) and (b) due to the limited extent of the local inversions. The region spanned in (a) is indicated in (b) by a white dashed line. A second dashed line indicates the base of the NSSL, $r_s = 0.946R$, defined as where the spherically-averaged Ω gradient changes sign.

we first fit the Ω profile to a functional form given by

$$\Omega(r, \theta) = \Omega_e(r) + \Omega_2(r) \cos^2 \theta + \Omega_4(r) \cos^4 \theta \quad (16)$$

and then compute the θ gradient analytically. We then compute the radial Ω gradient by means of a second-order finite difference scheme (on a non-uniform grid) applied to the fitting coefficients Ω_e, Ω_2, and Ω_4.

The estimation of $\mathcal{T}$ from equation (15) involves correlations between the mean meridional and zonal flow. For these we use the local inversions described in §4.1. In particular, we fit the local Ω inversion to a functional form as in equation (16) and the local $\langle v_\theta \rangle$ inversion (both from 1996) to a functional form given by

$$\langle v_\theta \rangle = \sin \theta \cos \theta \left(c_1(r) + c_3(r) \cos^2 \theta \right) \quad . \quad (17)$$

The fits to the local Ω and $\langle v_\theta \rangle$ inversions are plotted in Figures 3 and 2 as red dashed lines. The global Ω fit lies almost on top of these other curves and is thus omitted for clarity.

The mean radial velocity $\langle v_r \rangle$ is obtained by assuming mass conservation; $\boldsymbol{\nabla} \cdot \langle \rho \mathbf{v}_m \rangle = 0$. We also assume that $\rho \approx \langle \rho \rangle \approx \rho_s(r)$ where $\rho_s(r)$ is the spherically-symmetric mean density given by solar structure Model
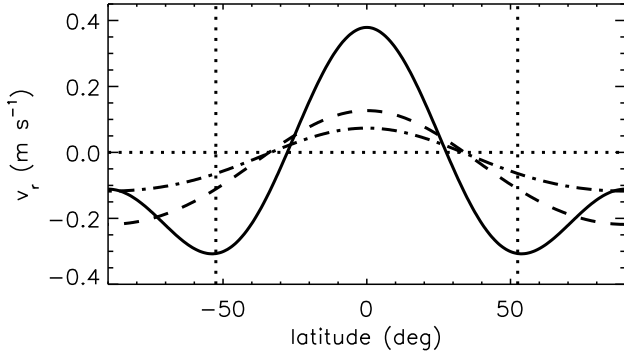
FIG. 5.— Mean radial velocity $\langle v_r \rangle$ inferred from mass conservation, based on local helioseismic inversions for $\langle v_\theta \rangle$. Solid, dashed, and dot-dashed lines correspond to $r = 0.977R$, $0.990R$, and $0.996R$ respectively. Dotted lines indicate zero velocity and the range in latitude spanned by the local inversions ($\pm$ 52.5°). Note that the curves extend beyond this range because they are based on the analytic expression given in equation (19).

S of Christensen-Dalsgaard et al. (1996). This gives

$$\frac{\partial}{\partial r}\left(r^2 \rho_s \langle v_r \rangle\right) = \frac{r\rho_s}{\sin\theta}\frac{\partial}{\partial\theta}\left(\sin\theta \langle v_\theta \rangle\right) \quad . \qquad (18)$$

The θ derivative on the right-hand-side of equation (18) is computed analytically from the fit in equation (17). This leads to the following form for $\langle v_r \rangle$

$$\langle v_r \rangle = w_e(r) + w_2(r)\cos^2\theta + w_4(r)\cos^4\theta \quad . \qquad (19)$$

We then proceed by expressing the radial derivative on the right-hand-side of equation (18) by means of a second-order finite difference scheme and we solve the resulting matrix equations for $r^2\rho_s w_i$ ($i = e, 2, 4$), with boundary conditions such that $\langle v_r \rangle = 0$ at $r = R$. The w_i are then smoothed using a boxcar window, taking into account the non-uniform grid. The resulting $\langle v_r \rangle$ profile is shown in Figure 5 for several radii.

Note that the amplitude of the inferred radial velocity is extremely small in the NSSL, less than 1 m s^{-1} and its contribution to $\mathcal{F}$ (and $\mathcal{T}$) is negligible. It does contribute a small positive maximum at the equator ($\sim 0.07 \times 10^8$ cm^2 s^{-1}) as seen in Figure 4a, but the prominent maximum at mid-latitudes is due almost entirely to the final term in equation (14), proportional to $\langle v_\theta \rangle \partial\mathcal{L}/\partial\theta$. Although there is some uncertainty in the estimation of $\langle v_r \rangle$ (§4.4), we believe this conclusion is robust. In order for the radial component to make a significant contribution to $\mathcal{F}$, the radial velocity would have to be at least an order of magnitude larger than our estimate. This would imply either a latitudinal velocity that is an order of magnitude larger, of order 200 m s^{-1}, or a latitudinal gradient of $\langle v_\theta \rangle$ that is an order of magnitude larger. If the amplitude of the meridional flow is to be no larger than 20 m s^{-1}, the requisite gradient would require that the peak flow be achieved within 3 degrees of the equator. Both scenarios can be ruled out by surface observations and helioseismic inversions.

Both $\mathcal{F}$ and $\mathcal{G}$ peak at mid-latitudes (Fig. 4) because this is where $\partial\Omega/\partial z$ and $\langle v_\theta \rangle \partial\mathcal{L}/\partial\theta$ peak. In fact, these two terms ($\partial\Omega/\partial z$ and $\langle v_\theta \rangle \partial\mathcal{L}/\partial\theta$) are identically zero at the equator because of the symmetry implied by equations (16) and (17). As emphasized in §5.4, this does not mean that the local angular and meridional momen-

tum flux must vanish at the equator, nor must the mean shear. Rather, it implies that the turbulent transport and the mean flows adjust themselves in such a way as to minimize the net zonal flux divergence (axial torque) $\mathcal{F}$ and the net meridional "force curl" $\mathcal{G}$. This is in contrast to mid-latitudes, where the net zonal and meridional momentum transport represented by $\mathcal{F}$ and $\mathcal{G}$ must be nonzero in order to balance the inertial forces associated with the mean differential rotation and meridional circulation. This delicate, nonlinear, nonlocal interplay between turbulent transport and mean flows ultimately determines the structure of the NSSL.

Note that the sign of $\mathcal{F}$ (and $\mathcal{T}$) is negative at mid-latitudes, signifying that turbulent stresses must exert a retrograde net axial torque, removing the angular momentum that is imparted by the meridional flow. The sign of $\mathcal{G}$, meanwhile, is positive, tending to induce a clockwise circulation in the northern hemisphere in order to offset the counter-clockwise circulation that would tend to establish a cylindrical (Taylor-Proudman) rotation profile (§3.2).

4.3. Anisotropy and Energetics

The quantities plotted in Figure 4, $\mathcal{T} = \mathcal{F}\rho^{-1}$ and $\mathcal{G}$, represent turbulent (non-axisymmetric) zonal and meridional momentum transport but a direct comparison between them is somewhat elusive since they apply in different contexts; $\mathcal{F}$ appears in the angular momentum equation while $\mathcal{G}$ appears in the zonal vorticity equation; their units are different. In this section we put $\mathcal{F}$ and $\mathcal{G}$ on an equal footing by converting them to accelerations, with units of cm s^{-2}. In other words, we can write the momentum equation as

$$\frac{\partial\langle\mathbf{v}\rangle}{\partial t} = -\left(\langle\mathbf{v}\rangle \cdot \boldsymbol{\nabla}\right)\langle\mathbf{v}\rangle + \frac{\boldsymbol{\nabla}\langle P\rangle}{\langle\rho\rangle} + \mathbf{A} \quad . \qquad (20)$$

Note that equation (20) is exact in the sense that it is faithful to the compressible MHD equations, with all non-axisymmetric influences (as well as some axisymmetric influences such as viscous diffusion and the mean-field Lorentz force) encapsulated in the "turbulent" acceleration term $\mathbf{A}$.

Now consider again our dynamical balance equations (2) and (11). The left-hand-side of both of these equations arises from the first term on the right-hand-side of equation (20), namely the inertia associated with mean flows (we use an inertial reference frame so the Coriolis force is included in this term as well; see Appx. A). The terms on the right-hand-side of equations (2) and (11), $\mathcal{F}$ and $\mathcal{G}$, arise from $\mathbf{A}$ so we can compute $\mathbf{A}$ from the helioseismic results presented in Figure 4. Note that the second term on the right-hand-side of equation (20) gives rise to the baroclinic term $\mathcal{B}$ in equations (8) and (10), which we propose is negligible in the NSSL (§3.3).

The zonal component of $\mathbf{A}$ is directly related to $\mathcal{F}$:

$$A_\phi = \frac{\mathcal{F}}{\lambda\rho} \quad . \qquad (21)$$

In order to obtain a relationship between $\mathcal{G}$ and the meridional components of $\mathbf{A}$, $\mathbf{A}_m$, we note that any arbitrary, axisymmetric vector field with only meridional
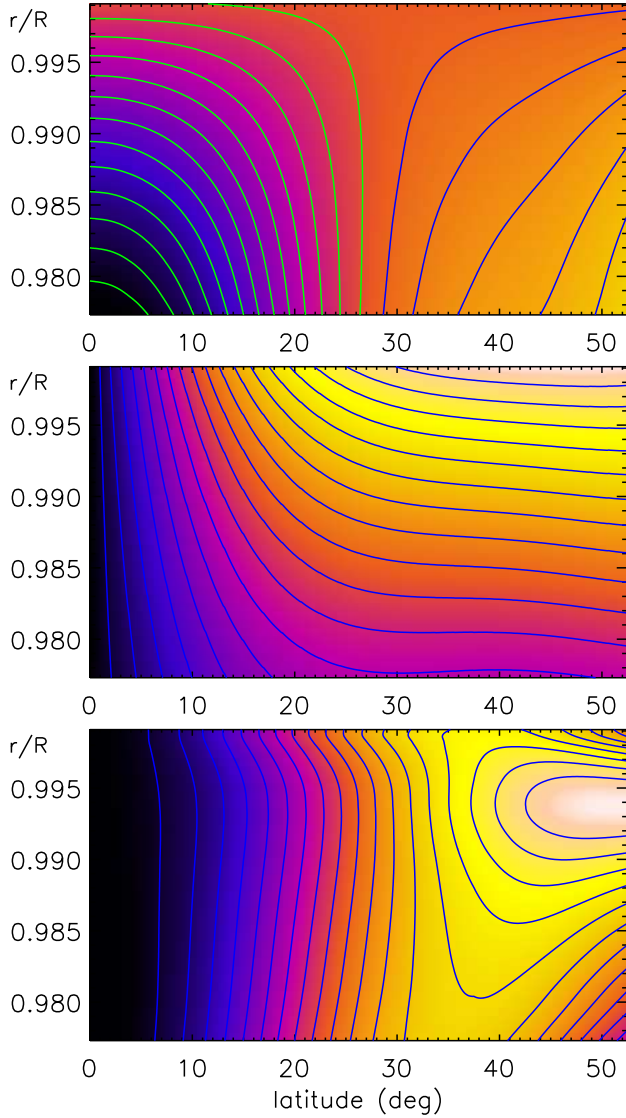
FIG. 6.— Acceleration terms (top) A_r, (middle) A_θ, and (bottom) $-A_\phi$, for the region spanned by the local inversions ($r > 0.978R$, lat $\leq 52.5°$). Scale ranges are $\pm 9 \times 10^{-4}$ cm s^{-2}, 0–2×10^{-2} cm s^{-2}, and 0–8×10^{-3} cm s^{-2} respectively, with colors ranging from black/blue to yellow/white. Blue contours denote positive values and green negative.

components can be represented as follows:

$$\mathbf{A}_m = \boldsymbol{\nabla} \times \left(\zeta \hat{\boldsymbol{\phi}} \right) + \boldsymbol{\nabla} \chi \quad, \tag{22}$$

where ζ and χ are functions of r and θ. The helioseismic estimate of $\mathcal{G}$ is obtained from the zonal vorticity equation and therefore provides no information about the compressible component, χ. However, taking the curl of equation (20) yields an equation for ζ:

$$(\boldsymbol{\nabla} \times \mathbf{A_m}) \cdot \hat{\boldsymbol{\phi}} = -\nabla^2 \zeta + \frac{\zeta}{\lambda^2} = \mathcal{G} \quad. \tag{23}$$

We solve this equation as described in Appendix C, subject to boundary conditions such that the radial acceleration vanish at the surface ($A_r = 0$ at $r = R$), and the latitudinal acceleration vanish at the base of the NSSL ($A_\theta = 0$ at $r = r_s$). The latter condition implies that the

TABLE 1
ENERGETICS AND TIME SCALES[a]

	$r > 0.978R$, lat $< 52.5°$	$r > 0.95R$ (extrapolated)
W_r	$-8.7 \times 10^{-8} L$	$-2.5 \times 10^{-6} L$
W_θ	$-1.3 \times 10^{-4} L$	$-4.7 \times 10^{-4} L$
W_ϕ	$-1.9 \times 10^{-2} L$	$-4.2 \times 10^{-2} L$
W_g	$8.9 \times 10^{-4} L$	$6.7 \times 10^{-3} L$
W_t	$-2.0 \times 10^{-2} L$	$-4.9 \times 10^{-2} L$
τ_s	200 days	590 days

[a] Work values are given in terms of the solar luminosity L.

latitudinal acceleration is relative to the deep CZ. The results are shown in Figures 6 and 7.

To facilitate comparison between the terms, the plotting range in Figure 6 is limited to that spanned by the local inversions. However, the results for A_r and A_θ extend to higher latitudes and deeper levels because they are based on the global inversions in Figure 1. This greater latitudinal extent is reflected in Figure 7, which also serves to illustrate the relative amplitudes and signs of each term.

The amplitudes of A_θ and A_ϕ peak at mid-latitudes while A_r is radially inward at the equator and outward above latitudes of about $26°$. As noted above with regard to Figure 4a, the zonal acceleration is negative, tending to decelerate the rotation rate in the NSSL. The positive sign of A_θ indicates an equatorward direction, tending to oppose the poleward meridional flow, thereby maintaining the rotational shear against Coriolis-induced circulations. The reversing sign of A_r, with an inward orientation at the equator also tends to oppose the meridional flow. This is consistent with the conceptual framework put forth in §2 and §3.

The amplitudes of A_θ and A_ϕ are comparable, which is remarkable because they are approximated by means of very different data sets and analysis techniques and represent distinct dynamical balances. The amplitude of the vertical acceleration is roughly an order of magnitude smaller than the horizontal components.

We can estimate the total rate of work done by each of the turbulent stress components as follows:

$$W_i = \int_V \rho_s \langle v_i \rangle A_i dV \qquad (i = r,\ \theta,\ \phi) \tag{24}$$

where V is the volume of the NSSL and ρ_s is again the spherically-symmetric density given by Model S. The results are listed in Table 1.

In the first column of Table 1, the volume V corresponds to the region spanned by the local helioseismic inversions and plotted in Figure 6. In the second column we extrapolate this to the entire NSSL, spanning $0.95R$–$1.00R$ in radius and pole-to-pole in latitude. The poleward extrapolations are based on the analytic fits expressed in equations (16) and (17), using global inversions for Ω and local inversions for $\langle v_\theta \rangle$.

When extrapolating A_ϕ in particular, we compute $\boldsymbol{\nabla}\mathcal{L}$ in equation (14) from global inversions interpolated onto the local helioseismic grid for $r \geq 0.977R$. We then extrapolate the expansion coefficients $c_1(r)$ and $c_3(r)$ that appear in (17), as shown in Figure 8, in order to obtain $\langle v_\theta \rangle$ and $\langle v_r \rangle$ down to $0.95R$. Slopes are chosen to flatten out below the matching point at $r = 0.977R$, anticipating an eventual flow reversal deeper in the CZ (we choose c_3
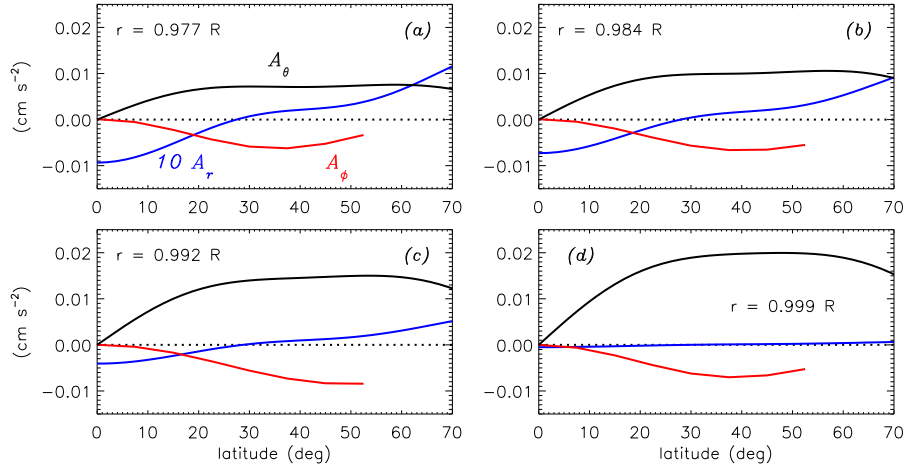
FIG. 7.— Acceleration terms A_r (dashed line, blue in online version), A_θ (solid black line), and A_ϕ (dot-dashed line; red in online version) as in Figure 6 but here plotted together versus latitude for several different radii, as indicated. The radial component A_r is multiplied by a factor of 10 for clarity of presentation. Note that we only show the A_ϕ curve out to 52.5° latitude because that is the extent of the local inversions used to compute it.
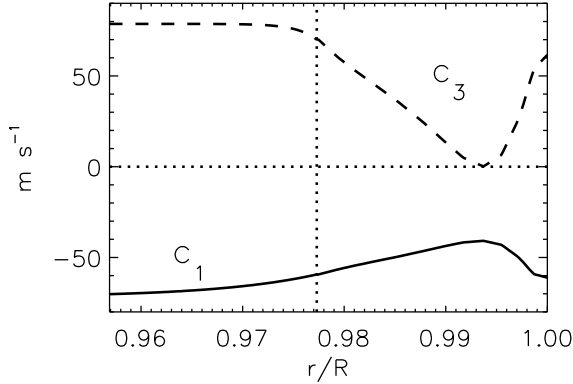

FIG. 8.— Radial variation of the expansion coefficients $c_1(r)$ (solid line) and $c_3(r)$ (dashed line), defined in equation (17). For $r > 0.977R$ (indicated by the vertical dotted line), the curves are based on fits to local helioseismic inversions. The extrapolations for $r < 0.977R$ are chosen to have continuous values and derivatives but flatter slopes as they extend deeper.

to flatten out somewhat more rapidly than c_1 in order to avoid high-latitude counter-cells resulting solely from the extrapolation). The numbers in Table 1 are not expected to be greatly sensitive to uncertainties in the meridional flow structure, unless the flow reversal actually occurs within the NSSL (§4.4).

The values in Table 1 indicate that the zonal force A_ϕ (corresponding to the net axial torque $\mathcal{F}$) does the most work, accounting for 2-4% of the solar luminosity. The work done by the latitudinal force A_θ is roughly two orders of magnitude smaller and that done by the radial force A_r is two to three orders of magnitude smaller still.

If the net axial torque $\mathcal{F}$ can be represented as the divergence of an angular momentum flux $\mathcal{F} = -\boldsymbol{\nabla}\cdot\mathbf{F}$, then the zonal work can be expressed as

$$W_\phi = \int_V \mathbf{F}\cdot\boldsymbol{\nabla}\Omega dV - \int_{\mathcal{S}} \Omega\mathbf{F}\cdot d\boldsymbol{\mathcal{S}} \equiv W_g + W_t \quad (25)$$

where $\mathcal{S}$ is the bounding surface of V, and $d\boldsymbol{\mathcal{S}}$ is directed normal to the surface. Here W_g is the work done against the angular velocity gradient and W_t is the work done

by means of transporting angular momentum through the surface $\mathcal{S}$. In a stationary state the mean mass flux is divergenceless, so equation (2) implies $\mathbf{F} = -\langle\rho\mathbf{v}_m\rangle\mathcal{L}$. The resulting values of W_g and W_t are listed in Table 1 and indicate that the latter dominates W_ϕ, accounting for its negative sign. Thus, most of the work done by turbulent stresses to maintain the NSSL against advection by the meridional flow involves transporting angular momentum out of the layer.

Our estimate for the angular momentum flux, $\mathbf{F}$, also allows us to compute a spin-down time scale for the NSSL:

$$\tau_s = \frac{\int_V \rho\mathcal{L}dV}{\int \mathbf{F}\cdot d\mathbf{S}} \quad . \qquad (26)$$

As indicated in Table 1, this suggest a value of about 200 days for the region spanned by the local inversions and about 590 days for the entire NSSL. This is comparable to the ventilation time

$$\tau_v \sim \frac{\pi R}{2V_\theta} \sim 630 \text{ days} , \qquad (27)$$

where $V_\theta \sim 20$ m s^{-1} is a typical meridional flow amplitude. This correspondence is not surprising since we estimated the turbulent angular momentum flux $\mathbf{F}$ based on the meridional flow.

4.4. Variability and Uncertainty

As mentioned in §1 and as demonstrated in §4.1 (Fig. 3), estimates of the meridional flow based on different observational data sets and different analysis techniques can vary substantially. Some of this variability can be attributed to measurement uncertainties but some is undoubtedly due to the intrinsic variability of the flow itself. In addition to the meridional flow, equations (2) and (8) also involve gradients in the angular velocity Ω which are also subject to measurement uncertainties and intrinsic variability. In this section we address what implications this variability and uncertainty has with regard to the principle arguments, results, and conclusions presented in this paper.

We begin with the physical processes discussed in sections 2 and 3. The predominant dynamical balances we advocate for the NSSL, represented by equations (2) and (11), are expected to hold regardless of the detailed amplitude and structure of the mean flows. They assume only that well-defined, persistent zonal and meridional flows exist when averaged over time intervals longer than a rotation period (of order one month) and that turbulent (i.e. Reynolds) stresses dominate over baroclinic forces ($\mathcal{G} >> \mathcal{B}$) in the NSSL.

Global rotational inversions indicate that variations in Ω over the solar cycle are not more than a few percent Thompson et al. (2003). Although Ω gradients may vary more than this (see below), they are not large enough to reverse the sign of $\partial \mathcal{L}/\partial \lambda$. In order to do so, relative variations in the rotation rate $\Delta\Omega/\Omega$ would have to exceed $2D/R$ where D is the length scale of the shear. Taking D to be the extent of the NSSL $\sim 0.05R$ implies variations with time of the zonal flow of at least several hundred m s^{-1}. Such large temporal variations can be ruled out based on photospheric observations and helioseismic rotational inversions (torsional oscillations are more like 20 m s^{-1}). Likewise, the uncertainty in ρ (obtained from Model S) is constrained by helioseismic structure inversions and is thus certain to within a few percent.

Thus, the principle source of uncertainty in the quantitative estimates presented in sections 4.2 and 4.3 is the meridional flow. Relative to zonal flow inversions, meridional flow inversions are subject to both greater measurement errors and greater intrinsic variability, by virtue of their weaker amplitude and asymmetric structure with respect to the equator (which precludes global inversions). Note that this source of uncertainty only effects our estimate for $\mathcal{F}$ and related quantities such as $\mathcal{T}$ in Fig. 4a, A_ϕ in Figures 6c and 7, and W_ϕ, W_g, W_t, and τ_s in Table 1. Our estimate for $\mathcal{G}$ and related quantities $(A_r, A_\theta, W_r, W_\theta)$ depends only on global rotation inversions, which are generally more reliable, particularly at high latitudes and large depths below the photosphere.

As noted in §4.2, the radial flow $\langle v_r \rangle$ makes a negligible contribution to our estimate of $\mathcal{F}$, even when the variability and uncertainty in the meridional inversion is taken into account. We have verified that this is consistent with our data by computing $\mathcal{T}$ for each of the years shown in Figures 2 and 3 (1996-2004). The amplitude of the radial component never exceeds 2×10^7 cm^2 s^{-1}, which is 5% of the saturation value of the color scale used in Figure 4a. The average amplitude is less than one percent of this saturation value.

The time variation of our $\langle v_\theta \rangle$ inversions varies greatly with latitude and depth, as shown in Figure 3. At latitudes less than 40° the standard deviation of these measurements is less than 50%. This is also the case for our estimate of $\mathcal{T}$, confirming that $\langle v_\theta \rangle$ is the principle source of uncertainty and variation. At latitudes greater than 40° and radii below $0.99R$ the inversions become less reliable and the standard deviation exceeds 50%.

However, we remind the reader that our quantitative estimates for $\mathcal{F}$ and related quantities in 4.2 and 4.3 are based on an analytic fit to the 1996 inversions, as shown by the dashed line in 3 (1996-2004). This is a smooth poleward flow with an amplitude of 18-21 m s^{-1} at all measured radii $r \geq 0.977R$. Although the amplitude of this flow is debatable, this general profile is consistent with the inpretation put forth by several authors who have argued that the spatial and temporal variation of the meridional flow can be interpreted as a persistent poleward background flow plus a time-dependent component associated with cyclic magnetic activity (e.g. Snodgrass & Dailey 1996; Basu & Antia 2010; Hathaway & Rightmire 2011). We are interested mainly in the background flow which is present throughout the solar cycle and is most prominent during solar minimum.

We emphasize that time averages of at least 2-3 months are needed to properly assess the mean flows we are concerned with here. That is the time scale over which the dynamical balances in equations (2) and (11) are established by means of the Coriolis force. Estimates of the meridional flow vary significantly from one Carrington rotation to the next, independent of the measurement technique. For example, the results of Hathaway & Rightmire (2010) based on feature tracking indicate that the amplitude of the dominant Legendre component can change by as much as 5 m s^{-1} over the course of one year. If one includes the higher-order components, the variation can be even larger, of order 5-10 m s^{-1} at the higher latitudes.

The importance of temporal averaging is evident when comparing our meridional flow inversions to those of Basu & Antia (2010), which are based on the same MDI data sets but each averaged over a single Carrington rotation. The natural variability in our measurements should be reduced from those of Basu & Antia by roughly a factor of 1.5 just due to our longer averages. Furthermore, our estimates are obtained by averaging over both longitude and time. At any given instant in time, we make 189 separate flow determinations scattered across the solar disk. All measurements made at the same latitude are then averaged together (15 determinations at the equator and 7 at the highest latitudes). The process is repeated on a daily basis and the results further averaged in time. Basu & Antia, on the other hand, only make estimates along the central meridian. So at high latitudes, even if the two teams average over a similar duration, we have 7 times more data going into the average. This high degree of temporal variability is the reason we used a representative smooth fit to the helioseismic measurements instead of directly using the measurements themselves.

According to our inversions, the amplitude of the background poleward flow is approximately 20 m s^{-1}. Other estimates based on various techniques including helioseismic inversions, Doppler measurements, and feature tracking generally range from 10-20 m s^{-1} (Snodgrass & Dailey 1996; Hathaway 1996; Haber et al. 2002; Zhao & Kosovichev 2004; Hindman et al. 2004; González-Hernandez et al. 2006; Ulrich 2010; Basu & Antia 2010; Hathaway & Rightmire 2010, 2011). If the mean meridional flow velocity were more like 10 m s^{-1} as suggested by feature tracking (e.g. Hathaway & Rightmire 2010), then our quantitative estimates for $\mathcal{T}$ in Figure 4a and A_ϕ in Figures 6c and 7 would be a factor of two too large. Furthermore, if the actual amplitude of $\langle v_\theta \rangle$ were to drop to zero near the base of the NSSL as suggested by Hathaway (2011), then our extrapolated values for W_ϕ, W_g, and W_t listed

in Table 1 would be overestimated.

With these variations and uncertainties in mind, we believe that our quantitative estimate for W_ϕ given in §4.3 is reasonable. In particular, since the meridional flow speed $\langle v_\theta \rangle$ is not likely to exceed 20 m s^{-1} through much of the NSSL ($r > 0.95R$), then the extrapolated value of W_ϕ is unlikely to exceed four percent of the solar luminosity, L. Moreover, since the average value of $\langle v_\theta \rangle$ throughout the NSSL ($r > 0.95R$) is not likely to be much less than 10 m s^{-1}, then W_ϕ is unlikely to be less than 1-2 percent of L.

Our estimate for $\mathcal{G}$ is based solely on global rotation inversions from 1996. Still, we can use the local inversions for the zonal flow shown in Figure 2 to estimate the temporal variation. This yields a standard deviation of less than 15% for latitudes less than 40°. The maximum standard deviation at the highest latitudes measured, 52.5° is 34%. This may be regarded as an upper limit to the uncertainty in the quantitative estimates for $\mathcal{G}$, A_r, A_θ, W_r, and W_θ in sections 4.2 and 4.3. We do not consider the time variation of global rotation inversions here but we expect they would imply smaller variations of $\mathcal{G}$ by virtue of their greater accuracy at higher latitudes and lower radii.

5. THE NATURE OF TURBULENT TRANSPORT

5.1. *Turbulent Diffusion and $\mathcal{L}$ Mixing*

Perhaps the simplest paradigm one can envision to potentially account for the existence of the NSSL is that of turbulent diffusion. In particular, one might suppose that as the length and time scales of the convection decrease drastically approaching the photosphere from below, the effects of rotation and spherical geometry become unimportant, so the convection becomes more homogeneous and isotropic, at least in the horizontal dimensions. Furthermore, given the small scale of the convective motions relative to the scale of the differential rotation and meridional circulation, one might expect them to suppress shear. The decrease in Ω near the surface may then be attributed to the vanishing of the Coriolis-induced velocity correlations that sustain the differential rotation deeper in the convection zone (in mean-field parlance, this would be the non-diffusive component of the Reynolds stress tensor, known as the Λ-effect; e.g. Rüdiger 1989). The NSSL would then be maintained by the outward diffusion of angular momentum from the deep convection zone together with the advection of angular momentum by the meridional flow. Is this paradigm consistent with observations?

An alternative paradigm introduced briefly in §1, is that photospheric convection tends to conserve angular momentum locally. This has been found repeatedly in numerical simulations of rotating convection in parameter regimes with weak rotational influence (high Rossby number, see: Gilman 1977; Gilman & Foukal 1979; Hathaway 1982; DeRosa et al. 2002; Aurnou et al. 2007; Augustson et al. 2011). In the absence of external forcing or boundary influences, turbulent mixing tends to establish a rotation profile such that $\mathcal{L}$ is uniform throughout the domain in question ($\Omega \propto \lambda^{-2}$). This is particularly evident in the recent simulations by Augustson et al. (2011) that employ open boundary conditions in the vertical, permitting convective motions to

pass through the boundaries.

In this section we consider these two paradigms for turbulent transport and investigate whether they are consistent with the helioseismic inversions discussed in §4. We will focus primarily on the angular momentum transport, represented by $\mathcal{F}$, and its implications with regard to the Ω profile. However, we emphasize again that the Ω profiles considered here can only be maintained with the help of corresponding meridional forces $\mathcal{G}$ or $\mathcal{B}$; these meridional forces are *required* to maintain rotational shear $\partial\Omega/\partial z$ *regardless* of the nature of $\mathcal{F}$.

For both paradigms, we express the net axial torque in terms of the divergence of a turbulent angular momentum flux: $\mathcal{F} = -\boldsymbol{\nabla} \cdot \mathbf{F}$. This is consistent with the hyperbolic nature of the compressible MHD equations and reliably captures the various components of $\mathcal{F}$, including the Reynolds stress, Lorentz force, and viscous diffusion (Appx. A).

In the case of turbulent diffusion, the form of the angular momentum flux $\mathbf{F}$ is analogous to that for molecular diffusion but the effective turbulent viscosity ν_t is many orders of magnitude larger than the molecular value. This yields

$$\mathcal{F} = -\boldsymbol{\nabla} \cdot \mathbf{F}_t = \boldsymbol{\nabla} \cdot \left(\rho \nu_t \lambda^2 \boldsymbol{\nabla} \Omega \right) \quad . \qquad (28)$$

Note that the direction of the angular momentum flux is down the gradient of Ω, $\mathcal{F}_t \propto -\boldsymbol{\nabla}\Omega$, tending to suppress rotational shear. By contrast, in our second paradigm, turbulence tends to mix angular momentum so we expect the flux to be down the gradient of $\mathcal{L}$:

$$\mathcal{F} = -\boldsymbol{\nabla} \cdot \mathbf{F}_a = \boldsymbol{\nabla} \cdot \left(\rho \nu_a \boldsymbol{\nabla} \mathcal{L} \right) \quad . \qquad (29)$$

where $\mathbf{F}_a \propto -\boldsymbol{\nabla}\mathcal{L}$. Given the $\mathcal{L}$ profile in Figure 1b, equation (29) produces an angular momentum flux that is radially inward and poleward, as in high-Rossby number convection simulations (e.g. DeRosa et al. 2002).

We emphasize that the motivation for equation (29) is purely phenomenological; this form is suggested by simulations of turbulent convection at high Rossby number. By contrast, equation (28) can be derived rigorously through the techniques of mean-field theory, assuming scale separation and that small-scale motions are homogeneous and isotropic.

We note also that the paper that introduced the concept of the near-surface shear layer, Foukal & Jokipii (1975; hereafter FJ75), touched on both paradigms. They represented the turbulent angular momentum flux as a viscous diffusion as in equation (28) with a constant dynamic viscosity $\rho\nu_t$. Substituting this into equation (2) and assuming a cylindrical rotation profile $\Omega = \Omega(\lambda)$ yields

$$\langle \rho v_\lambda \rangle \frac{d\mathcal{L}}{d\lambda} = -\boldsymbol{\nabla} \cdot \mathbf{F}_t = \frac{\rho \nu_t}{\lambda} \frac{d}{d\lambda} \left(\lambda^3 \frac{d\Omega}{d\lambda} \right) \quad . \qquad (30)$$

It is straightforward to show that this equation is the same as equation (1) in FJ75. They then consider the advection-dominated limit $\lambda v_\lambda >> \nu_t$ and argue that the flow will conserve angular momentum, yielding a profile $\mathcal{L} = $ constant.

However, it is important to note that FJ75 attributed the conservation of angular momentum to the *convection*, not to the mean flow. If $\mathcal{L}$ represents the axisymmetric zonal flow, then only the axisymmetric meridional flow

$\langle v_\lambda \rangle$ (assuming $\langle \rho v_\lambda \rangle \approx \langle \rho \rangle \langle v_\lambda \rangle$) will contribute to the advection term on the left-hand-side (lhs) of equation (30).

Thus, there are two ways to interpret the FJ75 result within the context of the two paradigms considered here. The first interpretation is that the turbulent angular momentum flux is diffusive in nature [eq. (28)] and the homogenization of angular momentum $\mathcal{L} \approx$ constant is achieved by means of the meridional flow. The second interpretation is that the $\langle v_\lambda \rangle$ and $\mathcal{L} = \lambda \langle v_\phi \rangle$ terms on the lhs of equation (30) represent not mean flows but rather convection; that is, replace the mean velocities with fluctuating velocities. When averaged over longitude and time, the net turbulent stress will then tend to homogenize $\mathcal{L}$, as expressed in (29).

Yet, both interpretations are incomplete in the sense that they do not take into account the observed poleward meridional flow which clearly crosses $\mathcal{L}$ contours as discussed in §4. The meridional flow does not conserve angular momentum on its own ($\langle \rho \mathbf{v}_m \rangle \cdot \boldsymbol{\nabla} \mathcal{L} \neq 0$), nor does the convection ($\mathcal{F} \neq 0$). Both must contribute to the subtle dynamical balances in the NSSL.

5.2. *Homogeneous Solutions and Stability*

In §5.1 we suggested two potential idealized forms for the turbulent angular momentum flux, expressed in equations (28) and (29). We now ask whether these paradigms are supported by helioseismic inversions. In this section we neglect the meridional flow and consider only the homogeneous solutions discussed in §2.2, equation (7). Namely, we calculate the Ω profile that would result in no net axial torque, $\mathcal{F} = 0$ and we ask whether this profile resembles the Ω profile deduced from helioseismology. Such solutions satisfy our zonal momentum equation (2) for $\langle \rho \mathbf{v}_m \rangle = 0$, as they must if they are to describe a steady state. We consider the influence of a meridional flow in §5.3.

We begin with the case of turbulent diffusion and we assume for simplicity that the density-weighted (dynamic) diffusion coefficent $\rho \nu_t$ is constant. Anisotropic and inhomogeneous diffusion coefficients will be considered in §5.4. From equation (28), the condition $\mathcal{F} = 0$ then requires

$$\boldsymbol{\nabla} \cdot \left(\lambda^2 \boldsymbol{\nabla} \Omega \right) = 0 \qquad \text{(turbulent diffusion)}. \qquad (31)$$

Similarly, if we assume $\rho \nu_a$ is constant, equation (29) yields

$$\nabla^2 \mathcal{L} = 0 \qquad (\mathcal{L} \text{ mixing}). \qquad (32)$$

In order to obtain solutions to equations (31) and (32) we must specify boundary conditions. Thus, to proceed, we must keep in mind the context in which these equations are proposed to be valid. They are intended to represent angular momentum transport in the NSSL alone; angular momentum in the deep convection zone (CZ) must be very different in order to sustain the solar differential rotation. Thus, to take into account the coupling between the NSSL and the deep CZ, we specify boundary conditions at the base of the NSSL.

It is often stated that the Ω contours at mid latitudes in the bulk of the CZ are nearly radial. Close scrutiny of Figure 1a reveals that Ω contours are not strictly radial; rather, they are tilted slightly toward the rotation axis so

$\partial \Omega / \partial r > 0$ in the bulk of the convection zone. However, in the NSSL, $\partial \Omega / \partial r < 0$. Thus, we define the base of the NSSL, r_s, as the radius at which the spherically-averaged radial Ω gradient passes through zero. This yields $r_s = 0.946$.

Thus, we solve equations (31) and (32) in the region $r_s \leq r \leq R$, subject to the boundary conditions $\partial \Omega / \partial r = 0$ and $\Omega = \Omega_s(\theta)$ at $r = r_s$. Here $\Omega_s(\theta)$ is an analytic fit as in equation (16) to the helioseismic inversions shown in Figure 1, interpolated to $r = r_s$. For further details on the boundary conditions and for the analytic solution of equations (31) and (32) see Appendix D. The results are plotted in Figure 9.

It is immediately apparent in Figure 9 that the actual Ω profile in the Solar NSSL inferred from helioseismology is steeper than suggested by either of the simple paradigms considered here. Not surprisingly, viscous diffusion tends to suppress shear so the equilibrium Ω profile in this case is nearly independent of radius. However, the latitudinal differential rotation is still prominent, roughly the same as at $r = r_s$ as a consequence of the thinness of the layer (coupled with the boundary conditions). Furthermore, a weak negative radial shear ($\partial \Omega / \partial r$) is established at high latitudes. This is a geometric effect associated with the inefficiency of viscous transport near the rotation axis ($\lambda = 0$).

The profile corresponding to $\mathcal{L}$ mixing [eq. (32)] is steeper than the diffusive profile, again as expected, since the direction of the flux ($\propto -\boldsymbol{\nabla} \mathcal{L}$) has a component that is radially inward. However, note that, within the context of the NSSL, *the concept of turbulent convection mixing angular momentum is not the same as turbulent convection establishing $\mathcal{L} = constant$*. The thin-shell geometry and the coupling of the NSSL to the rotation profile in the deep CZ (modeled here by means of our boundary conditions) preclude a complete homogenization of $\mathcal{L}$ even if the local convective transport were to exhibit that tendency.

At high latitudes, the Ω profile implied by $\mathcal{L}$ mixing is steeper and is more comparable to the helioseismic inversions. Both are less steep than the profile that would arise from a complete homogenization of $\mathcal{L}$. However, the helioseismic profile does approach homogenization in radius within about 7 Mm of the photosphere. In other words, the upper bound on the magnitude of $\partial \Omega / \partial r$ near the photosphere appears to be set by the Rayleigh stability criterion (Tassoul 1978)

$$\frac{\partial \mathcal{L}}{\partial \lambda} > 0 \qquad (\boldsymbol{\nabla} S = 0) \quad . \qquad (33)$$

Note that equation (33) is only strictly valid under the assumption that the stratification in the convection zone is approximately adiabatic ($\boldsymbol{\nabla} S = 0$). This is of course an oversimplication since the stratification in the NSSL is thought to be substantially superadiabatic. A more rigorous analysis indicates that the Rayleigh criterion (33) is part of a more general formulation of the Schwarzschild criterion for convective stability, which is clearly violated in a convection zone, essentially by definition. An independent stability criterion requires $\cos \theta (\boldsymbol{\nabla} S \times \boldsymbol{\nabla} \mathcal{L}) > 0$. However, if S isosurfaces are predominantly horizontal, then this provides no constraints on the radial shear in
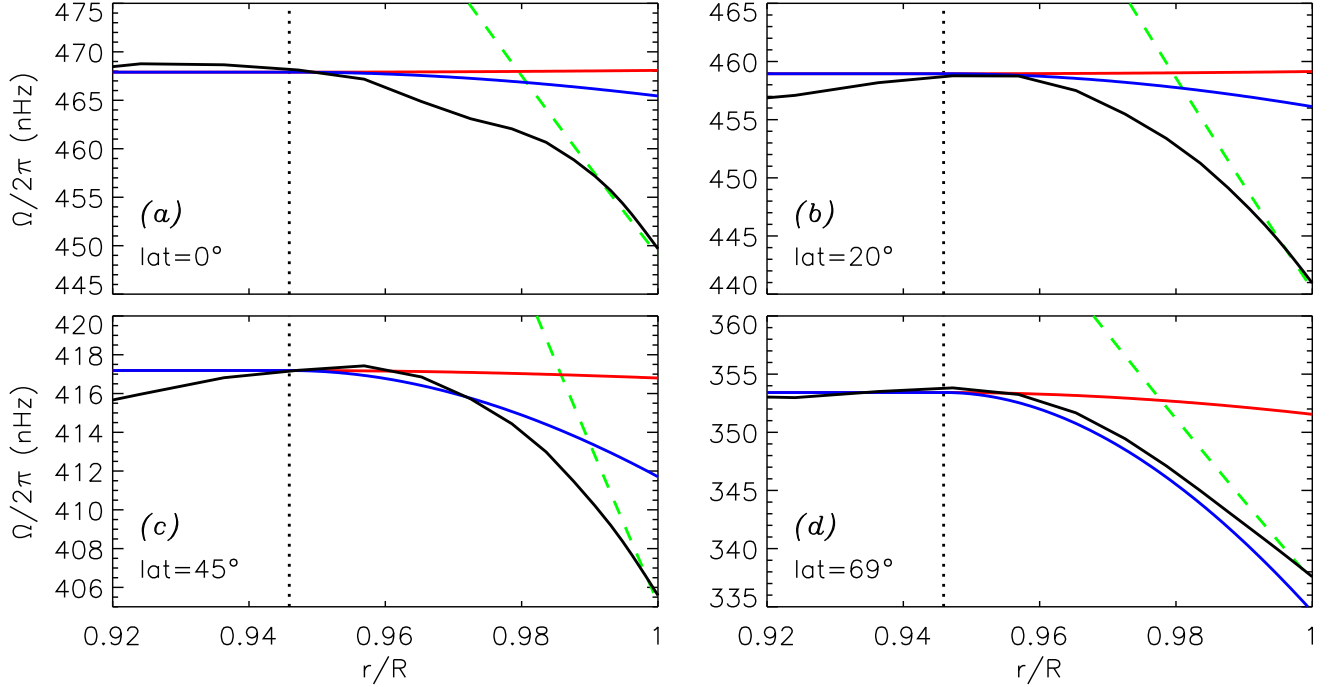
FIG. 9.— Rotation rate profiles are shown versus radius, spanning the upper convection zone ($0.92R \leq r \leq R$) for latitudes of (a) 0°, (b) 20°, (c) 45°, and (d) 69°. Dot-dashed lines (red in online color version of Figure) and dashed lines (blue in online version) represent viscous diffusion and $\mathcal{L}$ mixing respectively, obtained by solving equations equations (31) and (32) subject to the boundary conditions discussed in the text. Solid lines (black in online version) represent the helioseismic inversions shown in Fig. 1 and vertical dotted lines indicate the matching layer, $r = r_s$. The sloped dotted line (green dashed line in online version) represents an angular momentum profile that is independent of depth: $\mathcal{L} = \mathcal{L}_R(\theta)$ where $\mathcal{L}_R(\theta)$ is the surface value (at $r = R$).

the NSSL[2], $\partial\Omega/\partial r$. Both criteria arise from the Solberg-Høiland stability analysis as discussed, for example by Tassoul (1978). By considering the implications of equation (33) here, we are essentially separating out inertial effects from thermal effects, which may operate on different time scales. The potential relevance of this separation to the NSSL is supported by the remarkable correspondence between the maximum radial gradient of the helioseismic Ω profile and the slope implied by equation (33), as illustrated in Figure 9.

Thus, with these caveats, equation (33) implies that the radial Ω gradient near the photosphere is what it is because anything steeper would be unstable. Although this is indeed a compelling argument, it is well known that in the presence of a weak magnetic field the Rayleigh stability criterion is replaced by the stability criterion associated with the magneto-rotational instability (MRI). Thus, equation (33) is replace by the condition that $\partial\Omega/\partial\lambda > 0$ (Balbus 1995). This condition is clearly violated in the NSSL.

Why might the rotation profile be limited by the hydrodynamic Rayleigh criterion (33) yet violate the MRI stability criterion? There are two potential answers to this question. The first is that the MRI stability analysis may not be applicable in the NSSL. According to Balbus (1995), the assumptions that underlie the MRI criteria are valid for field strengths in the range $4\pi\rho\chi\Omega \ll B^2 \ll 4\pi\rho R^2\Omega^2$, where χ is the transport coefficient (in units of cm^2 s^{-1}) corresponding to the dominant diffu-

sive process. Dissipation in the NSSL is likely dominated by radiation and ohmic diffusion. The detailed physics is complicated and very sensitive to depth but nevertheless, rough estimates for the corresponding diffusion coefficients give $\kappa \sim 10^4$–10^5 cm^2 s^{-1} and $\eta \sim 10^6$–10^7 cm^2 s^{-1}. The κ value is derived from solar structure Model S (Christensen-Dalsgaard et al. 1996) and the η value follows from the Spitzer expression for a fully ionized Hydrogen plasma $\eta \sim 8 \times 10^{13}T^{-3/2}$ (Spitzer 1962). Using $\rho \sim 10^{-3}$ g cm^{-1}, we estimate that the MRI analysis of Balbus (1995) is valid for field strengths ranging from less than 1 G to more than 10^4G. The typical field strength in the NSSL is likely to lie within these bounds.

The second possibility is that the hydrodynamic Rayleigh instability is somehow more robust or more efficient than the MRI. Thus, the NSSL may indeed be unstable to MRI but the time scale of the instability (of order the rotation period ~ 28 days) is longer than the time scale over which the shear is established by turbulent stresses (of order the convective turnover time ~ 5 min – 1 day). Although this is plausible, the same argument would also in principle apply to the Rayliegh criterion so it is unclear why equation (33) must be satisfied while the MRI criterion is not. The depth over which the marginal slope is achieved, roughly within ~ 7 Mm of the photosphere, suggests that granulation may play a role. In any case, this is an interesting issue that should be explored further with the help of MHD convection simulations.

[2] In fact, it simply reflects convective instability since $\cos\theta(\partial S/\partial r)(\partial\mathcal{L}/\partial\theta) < 0$

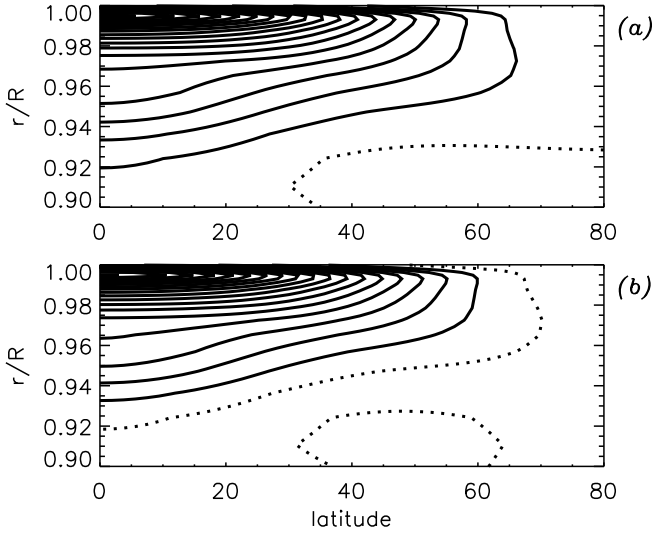### 5.3. Balancing the Meridional Flow

FIG. 10.— Differential operators applied to the (smoothed) solar Ω profile inferred from helioseismology (Fig. 1), corresponding to (a) viscous diffusion $\nabla \cdot (\lambda^2 \nabla \Omega_*)$ and (b) $\mathcal{L}$ mixing, $\nabla^2 (\lambda^2 \Omega_*)$. Solid lines denote negative values, dotted lines denote zero and positive values. The scaling is arbitrary since the corresponding torques depend on the unknown values of ν_t and ν_a.

The analysis presented in §5.2 assumes that the net torque $\mathcal{F}$ is zero, which is clearly not the case; as demonstrated in §4, observations imply that $\mathcal{F}$ is negative. Thus, we must take this into account if we are to properly assess whether our two simple paradigms for angular momentum transport can adequately account for the observed rotation and meridional flow profiles.

Stated another way, observations imply that the meridional flow is supplying angular momentum to the NSSL, tending to speed up the local rotation rate, while the turbulent transport must be removing angular momentum in order to maintain a stationary state. In order to assess whether turbulent diffusion or $\mathcal{L}$ mixing can provide the requisite transport, we must compute $\mathcal{F}$ from equations (28) and (29) based on the rotation profile inferred from helioseismology $\Omega_*(r, \theta)$ and ask whether it matches the inferred net axial torque shown in Figure 4a.

Of course, we cannot compute $\mathcal{F}$ explicitly because we do not know a priori the transport coefficients ν_t and ν_a. However, if we assume as in §5.2 that $\rho \nu_t$ and $\rho \nu_a$ are constant, then the corresponding torques, $\mathcal{F}_t$ and $\mathcal{F}_a$ will be proportional to the appropriate differential operators applied to the solar rotation profile, namely

$$\mathcal{F}_t \propto \nabla \left(\lambda^2 \nabla \Omega_* \right) \quad \text{and} \quad \mathcal{F}_a \propto \nabla^2 \left(\lambda^2 \Omega_* \right) \quad . \quad (34)$$

The right-hand-side of each of these equations is plotted in Figure 10.

The immediate impression from Figure 10 is that the two results look nearly identical. This is a consequence of the steepness of the radial Ω gradient and the thin-shell geometry. Thus, the dominant contribution to both operators is the second radial derivative:

$$\nabla \left(\lambda^2 \nabla \Omega_* \right) \approx \nabla^2 \left(\lambda^2 \Omega_* \right) \approx \lambda^2 \frac{\partial^2 \Omega_*}{\partial r^2} \quad . \quad (35)$$

As shown in Figure 9, the solar Ω profile is nearly flat at the base of the NSSL ($\partial \Omega / \partial r \approx 0$) and steepens with

increasing radius, reaching its maximum slope near the photosphere. Thus, $\partial^2 \Omega / \partial r^2 < 0$ and the quantities shown in Figure 10 are predominantly negative in the NSSL ($r > 0.95R$).

The negative sign of the quantities plotted in Figure 10 bodes well for the viability of our two simple paradigms for angular momentum transport. Both viscous diffusion and $\mathcal{L}$ mixing would tend to flatten out the negative curvature of the solar Ω profile ($\partial^2 \Omega / \partial r^2 < 0$). This would tend to decelerate the local rotation rate ($\mathcal{F} < 0$) and may thus serve to remove the angular momentum supplied to the NSSL by the meridional flow. The efficiency of the transport scales with the coefficients ν_t and ν_a and could be calibrated to give the proper net torque, at least in an integrated sense.

However, the profiles shown in Figure 10 are clearly different than the net axial torque profile inferred from helioseismic measurements, shown in Figure 4a. In particular, the idealized profiles in Figure 10 peak at the equator while the helioseismic profile in Figure 4a peaks at mid latitudes, with a weak positive signal at the equator. Thus, our simple paradigms appear to be inconsistent with helioseismic inversions. However, it may plausibly be argued that the assumption of homogeneous, isotropic coeffients $\rho \nu_t$ and $\rho \nu_a$ is unrealistic and unnecessary. In the next section we consider whether this can redeem our simple paradigms.

Before proceeding, we note in passing that the $\mathcal{L}$ mixing operator shown in Figure 10b suggests a reversal in the sign of the torque $\mathcal{F}$ at high latitudes. Since the local helioseismic inversions only extend up to latitudes of about 50°, we cannot determine whether a similar sign change occurs in the Sun. However, some measurements of the meridional flow suggest that there may be persistent high-latitude counter-cells, which are particularly apparent at solar minimum when magnetic effects can be more easily separated out (e.g. Ulrich 2010, see also Fig. 3). Under the justified assumption that the angular momentum continues to decrease toward the poles ($\partial \mathcal{L} / \partial \theta < 0$ in the northern hemisphere), equation (2) implies that a high-latitude counter-cell would indeed correspond to a change in sign of the net axial torque $\mathcal{F}$ (such that $\mathcal{F} > 0$).

5.4. Anisotropy and Inhomogeneity

The idealized rotation profiles and net axial torques considered in §5.2 and §5.3 are only valid for constant density-weighted transport coefficients $\rho \nu_t$ and $\rho \nu_a$. If one allows for inhomogeneous, anisotropic diffusion tensors then can the two paradigms considered here provide a better fit to helioseismic inversions?

This is to some extent a tautology; one might expect that one can construct a diffusion tensor to reproduce any arbitrary Ω and $\mathcal{F}$ profiles so the results of this analysis would not be very enlightening. However, we will demonstrate that turbulent diffusion can be ruled out as a viable paradigm even if it is anisotropic and inhomogeneous. Mixing angular momentum, on the other hand, may be more promising.

Note that, with regard to anisotropy, we are referring explicitly to the off-diagonal components of the viscous stress tensor ν_t or its $\mathcal{L}$-mixing analogue, ν_a. This should not be confused with the off-diagonal components of the Reynolds stress tensor, which are nonzero even for con-

stant scalar values of ν_t and ν_a. Indeed, the off-diagonal components of the Reynolds stress tensor are essential in order to account for the maintenance of mean flows.

Perhaps the most conspicuous fault with the profiles derived in §5.2 is that they admit an angular momentum flux through the solar surface. In the Sun, the sharp drop in density near the surface precludes any significant angular momentum flux through the photosphere on a time scale comparable to the convection turnover time or the rotation period. Angular momentum is lost through the solar wind but this loss rate is many orders of magnitude smaller than the rate at which angular momentum is continually circulated through the NSSL by convection and meridional flows.

Thus, we consider equation (28) again but we now allow for a diffusion coefficient that depends on radius. Furthermore, we allow for anisotropic transport so we can regard ν_t as a tensor. For the time being we will neglect the off-diagonal elements of the tensor so we can express ν_t in terms of vertical and horizontal component ν_{tv} and ν_{th}.

For $\rho\nu_{tv} = $ constant we found in §5.2 that the resulting Ω profile was too shallow to account for the helioseismic Ω profile. Can diffusion give rise to a steeper profile? The answer is yes, but only if the vertical diffusion $\rho\nu_{tv}$ increases with radius ($\partial(\rho\nu_{tv})/\partial r > 0$). This would provide an outward angular momentum flux that becomes larger closer to the solar surface, providing the requisite flux divergence to decelerate the NSSL. However, as pointed out in the previous paragraph, this cannot be sustained all the way to the photosphere where $\mathbf{F}$ and thus $\rho\nu_{vt}$ must drop to zero.

To demonstrate that even an anisotropic, inhomogeneous diffusion cannot account for the NSSL consider a closed volume V bounded from below by the surface $r = r_b$ and from above by the photosphere R. Latitudinal boundaries are at the equator and at an arbitrary colatitude θ_0, located in the northern hemisphere close enough to the equator to be accessible to helioseismic inversions, say $\pi/6 < \theta_0 < \pi/2$ (corresponding to a latitude between 0 and 60°). We now integrate the net axial torque $\mathcal{F}$ over the volume, allowing for anisotropic transport and assuming $\mathbf{F} = 0$ at $r = R$. The symmetry of the Ω profile implies no angular momentum flux through the equatorial plane ($\partial\Omega/\partial\theta = 0$) so the integrated torque is given by

$$\int_V \mathcal{F}dV = -\int_{\mathcal{S}} \mathbf{F}\cdot d\mathcal{S} \qquad (36)$$

$$= -2\pi \left[r_b^4 \int_{\theta_0}^{\pi/2} \rho\nu_v \frac{\partial\Omega}{\partial r}\sin^3\theta d\theta + \int_{r_b}^R \rho\nu_h \frac{\partial\Omega}{\partial\theta}r^2 dr \right]$$

where $\mathcal{S}$ is the bounding surface, and the first and second terms on the right-hand-side are to be evaluated at $r = r_b$ and $\theta = \theta_0$ respectively.

As discussed in §4 and §5.3, the integral in equation (36) must be negative. However, if we choose r_b to lie within the NSSL, then $\partial\Omega/\partial r < 0$ and the first term is positive. In other words, angular momentum flux into the NSSL through the lower surface $r = r_b$ must be shunted poleward in order to be consistent with a negative (or zero) net torque $\int_V \mathcal{F}dV$. Although the latitudinal flux is indeed poleward ($\partial\Omega/\partial\theta < 0$ at $\theta = \theta_b$), it

cannot be efficient enough to maintain a negative $\partial\Omega/\partial r$ throughout the NSSL. As r_b approaches R from below, the second term in brackets can be approximated by $\rho\nu_h R^2(R - r_b)(\partial\Omega/\partial\theta)$. In order to transport the requisite flux, the viscosity anisotropy ν_h/ν_v would have to increase radially without bound, becoming infinite at the photosphere.

This argument can be readily generalized to rule out any arbitrary outward flux $\mathbf{F}\cdot\hat{\boldsymbol{r}} > 0$. The implication, then, is that *the angular momentum flux in the NSSL must be radially inward.* One can in principle salvage the diffusive paradigm if one invokes negative diffusion or the off-diagonal elements of the turbulent viscosity tensor, namely an inward angular momentum flux that is proportional to the latitudinal shear. However, such prescriptions seem rather contrived.

Thus, we can confidently say that the turbulent transport in the NSSL cannot be adequately modeled as a turbulent diffusion. How does our other paradigm fare, namely that of mixing angular momentum?

We can see immediately that this paradigm is more plausible because the angular momentum transport is indeed inward $\mathbf{F}\cdot\hat{\boldsymbol{r}} < 0$. A steeper $\partial\Omega/\partial r$ profile could then be achieved by means of a diffusion coefficient $\rho\nu_a$ that decreases with radius ($\rho\nu_a$), approaching zero at the photosphere, as required by the condition $\mathbf{F} = 0$ at $r = R$. Thus, the $\mathcal{L}$-mixing paradigm is consistent with both an inward Ω gradient ($\partial\Omega/\partial r < 0$) and no net angular momentum flux through the photosphere.

However, in order to be consistent with the form of the net axial torque inferred from helioseismology, the density-weighted mixing coefficient $\mu = \rho\nu_a$ would have to have a very particular form. As shown in Figure 4a, the net axial torque is nearly zero at the equator whereas $\nabla^2\mathcal{L}$ has a prominent peak at the equator (Fig. 10b). In order to see how this may be remedied, assume that μ is isotropic but varies with radius with a scale height much less than the solar radius R. Furthermore, assume as in equation (4) that the $\mathcal{L}$ profile is nearly cylindrical. Then equation (29) yields

$$\mathcal{F} \approx \mu\nabla^2\mathcal{L} + 2\sin\theta\frac{d\mu}{dr}\frac{d\mathcal{L}}{d\lambda} + \mathcal{L}\frac{d^2\mu}{dr^2} \quad . \qquad (37)$$

If $\mu = \rho\nu_a$ decreases with increasing radius as suggested in the previous paragraph, then inserting the helioseismic value for $\mathcal{L} = \lambda^2\Omega_*$ implies that the first two terms are negative at the equator. In other words, the sharp decrease of μ exacerbates the prominent negative net torque $\mathcal{F}$ seen in Figure 10b. One way out of this dilemma is if the slope flattens out near the photosphere so $d^2\mu/dr^2 > 0$. Then the last term in equation (37) is positive and correspondence with Figure 4a becomes possible.

In summary, helioseismology sets fairly strict constraints on the nature of the turbulent angular momentum flux $\mathbf{F}$ in the NSSL, including: (1) $\mathbf{F}$ must be radially inward ($\mathbf{F}\cdot\hat{\boldsymbol{r}} < 0$), (2) there must be no flux through the photosphere ($\mathbf{F}\cdot\hat{\boldsymbol{r}} = 0$ at $r = R$), (3) $\mathbf{F}$ must diverge at mid-latitudes ($\mathcal{F} < 0$) in order to balance the advection of angular momentum by the meridional flow, and (4) turbulent transport at low latitudes must redistribute angular momentum in such a way as to support a steep radial Ω gradient while minimizing the net axial torque

($\mathcal{F} = \boldsymbol{\nabla} \cdot \mathbf{F} = 0$). The turbulent diffusion paradigm, equation (28), does not meet these constraints and is therefore not a valid model of turbulent transport in the NSSL. The alternative ansatz of $\mathcal{L}$ mixing, as expressed in equation (29), is at least feasible, but it would require a fine-tuned, inhomogeneous and/or anisotropic mixing coefficient $\mu = \rho \nu_a$. For example, it could in principle be achieved with a vertical mixing coefficient that decreases with radius but flattens out near the photosphere ($\partial \mu / \partial r < 0$, $\partial^2 \mu / \partial r^2 > 0$). A power law dependence $\mu \propto r^n$ with $n < 0$ may satisfiy such a requirement. However, it is more likely that the turbulent Reynolds stress in the NSSL is more complex than either of these crude, local models.

5.5. *Meridional Momentum Transport*

Despite the conclusion of section §5.4 regarding the non-diffusive nature of $\mathcal{F}$, it is reasonable to expect that $\mathcal{G}$ may operate essentially as a turbulent diffusion. In order to appreciate why this may be the case, consider again the time-dependent thought experiment discussed in §3.2. Here we begin with a spherical volume V in uniform rotation and a retrograde torque $\mathcal{F}$ is introduced in the surface layers ($r > 0.95$). This will establish a poleward flow $\langle v_\theta \rangle$ which will steadily increase in amplitude, striving to establish a cylindrical rotation profile as discussed in §3.2. Given the thin-shell geometry of the NSSL, one may expect strong vertical gradients $\partial v_\theta / \partial r$ to be established. Furthermore, given the small scale of photospheric convection relative to the mean flow, one may expect turbulent stresses to resist such shearing motions. This would imply that the resulting axial differential rotation profile $\partial \Omega / \partial z$ is determined by how efficiently small-scale convective motions can mix latitudinal momentum, $\langle v_\theta \rangle$, or equivalently, suppress zonal vorticity, $\langle \omega_\phi \rangle$.

Thus, under this scenario we may expect that $\mathcal{G}$ will be diffusive (down-gradient) in nature, and furthermore, that the strain rate tensor will be dominated by vertical gradients in the poleward flow. The turbulent transport would then be given by

$$\mathcal{G} \sim \nu_t \frac{\partial^2 \omega_\phi}{\partial r^2} \sim \nu_t \frac{\partial^3 v_\theta}{\partial r^3} \quad , \tag{38}$$

where ν_t is again the turbulent (kinematic) viscosity. Note that this expression assumes that the scale of variation of the dynamic viscosity $|d \ln(\rho \nu_t)/dr|^{-1}$ is larger than that of the shear $|d \ln |v_\theta|/dr|^{-1}$.

Equation (38) can in principle provide the momentum transport required to balance the Coriolis force associated with the axial shear $\partial \Omega / \partial z$. However, this is contingent on the amplitude of v_θ being strongly peaked near the photosphere, such that $\partial^3 |v_\theta|/\partial r^3 < 0$. This does not appear to be supported by local helioseismic inversions (§4), but the sensitivity and resolution of the inversions is likely not adequate enough to provide reliable estimates for third-order derivatives of v_θ (e.g. Beckers 2007; Hathaway 2011). An alternative is that the dynamic turbulent viscosity $\rho \nu_t$ decrease with radius while the velocity amplitude increase, consistent with no tangential stress at the photosphere.

In summary, we can say that if the turbulent transport $\mathcal{G}$ does indeed dominate over baroclinic forcing $\mathcal{B}$ as sug-

gested in §3.3 then it must resist the poleward meridional flow induced by $\mathcal{F}$ through the Coriolis force. Thus, $\mathcal{G}$ must be negative in the northern hemisphere and positive in the southern hemisphere. A turbulent diffusion or similar mixing process may be adequate, as would a more general formulation.

6. SUMMARY AND CONCLUSION

6.1. *Maintenance of the Solar NSSL*

We have demonstrated that the turbulent angular momentum transport in the solar Near-Surface Shear Layer (NSSL) is responsible for the persistent poleward meridional flow but it does not uniquely determine the mid-latitude Ω profile. Rather, the axial rotation gradient $\partial \Omega / \partial z$ must be maintained by turbulent stresses in the meridional plane. More specifically, a retrograde zonal force (axial torque) $\mathcal{F} < 0$ establishes the NSSL and regulates the poleward meridional flow while meridional forcing regulates the mid-latitude Ω profile. Furthermore, we argue that a transition in the meridional force balance from baroclinic to turbulent stresses [$\mathcal{B}$ to $\mathcal{G}$ in equation (8)] may determine the base of the NSSL.

More generally, we have demonstrated that there is close dynamical relationship between the differential rotation and the meridional circulation and that the structure of the NSSL as inferred from helioseismology relies on a delicate nonlinear, nonlocal interplay between the two. The same physical mechanism ($\mathcal{F} < 0$) that establishes negative radial shear $\partial \Omega / \partial r < 0$ also establishes poleward flow ($\langle v_\theta \rangle < 0$ in the northern hemisphere). As suggested by previous authors, we attribute this physical mechanism to Reynolds and possibly Maxwell stresses associated with the relatively small-scale convection (granulation to supergranulation) that permeates the NSSL.

Throughout our analysis, we have considered the inertia of the mean flow explicitly, incorporating other physical processes in the generalized zonal and meridional forcing terms $\mathcal{F}$ and $\mathcal{G}$ which we refer to as turbulent stresses. This is intended to clarify the essential physics of how the differential rotation and meridional circulation are coupled in their response to zonal and meridional forcing, independent of the detailed nature of this forcing, which is unknown. The reader may wish to regard $\mathcal{F}$ and $\mathcal{G}$ simply as the the convective Reynolds stress, since this is likely to be their dominant component (Appendix A). However, as noted in the introduction, other forcing such as large-scale Lorentz forces and viscous diffusion can induce mean flows in an analogous way.

We have demonstrated that turbulent transport in the NSSL is non-diffusive in nature and must be directed radially inward (§5). Inspired by numerical simulations of turbulent convection at large Rossby numbers, we have considered an alternative paradigm for turbulent transport based on the mixing of specific angular momentum, $\mathcal{L}$. We have shown that the conservation of angular momentum alone cannot account for the existence of the NSSL (§3) but the form of the rotation profile may be consistent with $\mathcal{L}$ mixing if the mixing coefficient is inhomogeneous and/or anisotropic (§5). Furthermore, we have shown that $\mathcal{L}$ mixing is a more general concept than simply $\mathcal{L}$-homogenization (constant $\mathcal{L}$) when one takes into account the coupling between the NSSL and the deep convection zone. Yet, the failure of simple tur-

bulent diffusion or $\mathcal{L}$-mixing prescriptions demonstrates that the NSSL is not simply a passive response to deeper forcing; it must be actively maintained by anisotropic and inhomogeneous turbulent transport.

Estimates based on local and global helioseismology indicate that it takes 2–4% of the solar luminosity to maintain the NSSL against the inertia of the mean flow (§4.3). Most of this work is associated with transporting angular momentum out of the layer (W_t in Table 1) in order to balance the convergence of angular momentum flux into the layer by meridional flow advection. The estimated amplitudes of turbulent transport in the latitude and longitude directions (A_θ and A_ϕ) are remarkably similar, given the very different way in which these two quantities were obtained (the former follows from "uncurling" global Ω inversions while the latter involves estimates of zonal and meridional flows from local helioseismology; see §4.3). The vertical transport in the middle of the NSSL is about an order of magnitude less (at the base of the NSSL, $r = r_s$, A_θ is zero by assumption and our local helioseismic inversions provide no information on A_ϕ). The sense of all these terms is such that turbulent transport is decelerating the rotation rate in the NSSL and opposing the meridional flow.

Estimates of the spin-down time scale indicate that it is similar to the ventilation time scale of about 600 days (§4.3). This is long compared to the turnover time scale of convective motions, $\lesssim 1$ day, implying that the net turbulent angular momentum transport is rather inefficient.

Finally, we note that the upper limit to the slope of the radial Ω gradient appears to be set by the Rayleigh criterion, equation (33). However, it is unclear why this intrinsically hydrodynamic condition should be satisfied in the NSSL while its MHD analogue, the stability criterion for the magnetorotational instability (MRI) $\partial\Omega/\partial\lambda > 0$, is clearly violated.

6.2. *Implications for Numerical Models*

Several authors have sought to investigate the dynamics of the NSSL through numerical simulations of solar convection in thin spherical shells or spherical segments, placing the lower boundary of the simulation domain within the upper convection zone, typically above $0.9R$ (e.g. Gilman & Foukal 1979; Hathaway 1982; DeRosa et al. 2002; Augustson et al. 2011). Relative to global simulations spanning the entire convection zone, these have the great advantage that smaller scales can be resolved so the turbulent transport can be more reliably captured. Although these simulations have provided insight into the dynamics of the NSSL, none have accurately reproduced the angular velocity profile throughout the NSSL. As we have demonstrated here, the dynamics of the NSSL involves a delicate balance between small-scale turbulent transport, large-scale mean flows, and coupling to the deep convection zone (CZ). Even if thin-shell models properly capture the turbulent transport, they must also capture or otherwise mimic the coupling to the CZ if they are to achieve solar-like mean flows.

A straightforward and common strategy in thin-shell models is to impose a solar-like latitudinal differential rotation on the lower boundary (e.g. Gilman & Foukal 1979; DeRosa et al. 2002). If the lower boundary is also impermeable, as is often the case, then it is clear

that the system cannot sustain a poleward flow throughout the layer. What implications might this have for the differential rotation? As is demonstrated in §4, the meridional circulation supplies angular momentum to the NSSL while turbulent stresses must remove this angular momentum. This balance, together with the meridional stresses $\mathcal{G}$ (or $\mathcal{B}$) determine the mean flow profiles. If the poleward flow is artificially suppressed by an impenetrable boundary condition, then there must be alternative source of angular momentum to balance turbulent transport. Without this source, the Ω profile will be adversely affected in addition to the meridional flow profile.

The rotational coupling between the convection zone and the NSSL in this class of numerical models is achieved by means of viscous diffusion. This is artificial in the sense that the viscosity used is many orders of magnitude larger than that of the solar plasma. However, can this effectively mimic the coupling that is expected to occur in the Sun? On the positive side, viscous coupling can indeed serve as an angular momentum source, allowing the integrated turbulent stresses $\int_V \mathcal{F}dV$ throughout the NSSL to be negative, as in the Sun. However, the latitudinal distribution of the viscous torques is likely to be very different than for gyroscopic pumping. If $\partial\Omega/\partial r < 0$ at nearly all latitudes in the solar NSSL as implied by helioseismic inversions (although these are uncertain poleward of 70°), then viscous coupling would imply outward angular momentum transport everywhere. By contrast, the meridional flow would impart angular momentum at low latitudes and remove it at high latitudes in such a way that the net convergence into the layer is positive. This implies a high-latitude angular momentum flux that may be up the gradient of Ω. One would expect the resulting Ω profile to be very different than for viscous coupling. Mean flow profiles would be similarly sensitive to impermable boundary conditions in latitude.

Thus, in order to properly model the NSSL, numerical models must either be deep enough to capture the closed meridional circulation, including the poleward flow at the surface and the return equatorward flow, or they must impose boundary conditions that are conducive to establishing solar-like mean flows. These may include open boundaries on which the rotation profile Ω is specified in addition to an imposed net axial torque $\mathcal{F}$, chosen to induce a commensurate meridional flow through the boundary by means of gyroscopic pumping, as expressed by equation (2).

Even if the simulation domain is in principle large enough to capture the complete, closed meridional circulation, the delicate balance expressed in equation (2) implies that the meridional flow is particularly sensitive to artificial viscous dissipation. If viscous angular momentum transport largely balances the angular momentum transport by the convective Reynolds stress as in many numerical models, then $\mathcal{F}$ will nearly vanish and the meridional flow may be very different than what occurs in the Sun (Miesch et al. 2008, 2011). Regardless of the boundary conditions, realistic meridional flow profiles require minimal viscous dissipation.

REFERENCES

Augustson, K., Rast, M., Trampedach, R., & Toomre, J. 2011, J. Phys. Conf. Ser., 271, 012070
Aurnou, J., Heimpel, M., & Wicht, J. 2007, Icarus, 190, 110
Balbus, S. A. 1995, ApJ, 453, 380
Basu, S. & Antia, H. M. 2010, ApJ, 717, 488
Beck, J. G., Gizon, L., & Duvall, T. L. 2002, ApJ, 575, L47
Beckers, J. 2007, Solar Physics, 240, 3
Braun, D. C. & Fan, Y. 1998, ApJ, 508, L105
Brun, A. S., Antia, H. M., & Chitre, S. M. 2010, Astron. Astrophys., 510, A33
Brun, A. S., Miesch, M. S., & Toomre, J. 2011, Modeling the Dynamical Coupling of the Solar Convection Zone to the Radiative Interior, apJ, submitted
Brun, A. S. & Toomre, J. 2002, ApJ, 570, 865
Chou, D.-Y. & Dai, E.-C. 2001, ApJ, 559, L175
Christensen-Dalsgaard, J. 2002, Rev. Mod. Phys., 74, 1073
Christensen-Dalsgaard, J. et al. 1996, Science, 272, 1286
DeRosa, M. L., Gilman, P. A., & Toomre, J. 2002, ApJ, 581, 1356
Elliott, J. R., Miesch, M. S., & Toomre, J. 2000, ApJ, 533, 546
Foukal, P. & Jokipii, J. R. 1975, ApJ, 199, L71
Garaud, P. & Arreguin, L. A. 2009, ApJ, 704, 1
Garaud, P. & Bodenheimer, P. 2010, ApJ, 719, 313
Garaud, P. & Brummell, N. H. 2008, ApJ, 674, 498
Giles, P. M. 1999, Time-Distance Measurements of Large-Scale Flows in the Solar Convection Zone, ph.D. Thesis, Stanford Univ., Stanford, USA http://soi.stanford.edu/papers/dissertations/giles/thesis/PDF
Giles, P. M., Duvall, T. L., Scherrer, P. H., & Bogart, R. S. 1997, Nature, 390, 52
Gilman, P. A. 1977, Geophys. Astrophys. Fluid Dyn., 8, 93
Gilman, P. A. & Foukal, P. V. 1979, ApJ, 229, 1179
Gilman, P. A. & Miesch, M. S. 2004, ApJ, 611, 568
González-Hernandez, I., Komm, R., Hill, F., Howe, R., Corbard, T., & Haber, D. A. 2006, ApJ, 638, 576
Gough, D. O. & McIntyre, M. E. 1998, Nature, 394, 755
Gough, D. O. et al. 1996, Science, 272, 1296
Haber, D. A., Hindman, B. W., & Toomre, J. 2002, ApJ, 570, 855
Haber, D. A., Hindman, B. W., Toomre, J., & Thompson, M. J. 2004, Solar Physics, 220, 371
Hathaway, D. H. 1982, Solar Phys., 77, 341
—. 1996, ApJ, 460, 1027
—. 2011, The Sun's Shallow Meridional Circulation, arXiv:1103.1561
Hathaway, D. H. & Rightmire, L. 2010, Science, 327, 1350
—. 2011, ApJ, 729, 80
Haynes, P. H., Marks, C. J., McIntyre, M. E., Shepherd, T. G., & Shine, K. P. 1991, J. Atmos. Sci., 48, 651
Hill, F. 1988, ApJ, 333, 996
Hindman, B. W., Gizon, L., Duvall, T. L. Jr., Haber, D. A., & Toomre, J. 2004, ApJ, 1253

Howe, R. 2009, Living Reviews in Solar Physics, 6, http://www.livingreviews.org/lrsp-2009-1
Howe, R., Christensen-Dalsgaard, J., Hill, F., Komm, R. W., Larsen, R. M., Schou, J., Thompson, M. J., & Toomre, J. 2000, Science, 287, 2456
Hughes, D. W., Rosner, R., & Weiss, N. O., eds. 2007, The Solar Tachocline (Cambridge: Cambridge Univ. Press)
Kitchatinov, L. L. & Rüdiger, G. 1995, A&A, 299, 446
McIntyre, M. E. 1998, Prog. Theor. Phys. Supl., 130, 137, corrigendum, Prog. Theor. Phys., 101, 189 (1999).
McIntyre, M. E. 2007, in The Solar Tachocline, ed. D. W. Hughes, R. Rosner, & N. O. Weiss (Cambridge: Cambridge Univ. Press), 183–212
Miesch, M. S., Brown, B., Browning, M., Brun, A., & Toomre, J. 2011, in Proc. IAU Symp. 271, "Astrophysical Dynamics: From Stars to Galaxies, ed. N. Brummell, A. S. Brun, M. S. Miesch, & Y. Ponty (Cambridge: Cambridge Univ. Press), in press
Miesch, M. S., Brun, A. S., DeRosa, M. L., & Toomre, J. 2008, ApJ, 673, 557
Miesch, M. S., Brun, A. S., & Toomre, J. 2006, ApJ, 641, 618
Miesch, M. S. & Toomre, J. 2009, Ann. Rev. Fluid Mech., 41, 317
Nordlund, A., Stein, R. F., & Asplund, M. 2009, Living Reviews in Solar Physics, 6, http://www.livingreviews.org/lrsp-2009-2
Pedlosky, J. 1987, Geophysical Fluid Dynamics, 2nd edn. (New York: Springer-Verlag)
Rast, M. P., Ortiz, A., & Meisner, R. W. 2008, ApJ, 673, 1209
Rempel, M. 2005, ApJ, 622, 1320
Rempel, M. 2007, ApJ, 655, 651
Robinson, F. J. & Chan, K. L. 2001, MNRAS, 321, 723
Rüdiger, G. 1989, Differential Rotation and Stellar Convection (New York: Gordon and Breach)
Schou, J., Howe, R., Basu, S., Christensen-Dalsgaard, J., Corbard, T., Hill, F., Komm, R., Larsen, R. M., Rabello-Soares, M. C., & Thompson, M. J. 2002, ApJ, 567, 1234
Snodgrass, H. B. & Dailey, S. B. 1996, Solar Phys., 163, 21–42.
Spiegel, E. A. & Zahn, J.-P. 1992, Astron. Astrophys., 265, 106
Spitzer, L. 1962, Physics of Fully Ionized Gases, 2nd edn. (New York: Interscience)
Spruit, H. C. 2003, Solar Phys., 213, 1
Tassoul, J. L. 1978, Theory of Rotating Stars (Princeton: Princeton Univ. Press)
Thompson, M. J., Christensen-Dalsgaard, J., Miesch, M. S., & Toomre, J. 2003, ARA&A, 41, 599
Thompson, M. J. et al. 1996, Science, 272, 1300
Ulrich, R. K. 2010, ApJ, 725, 658
Zhao, J. & Kosovichev, A. G. 2004, ApJ, 603, 776

APPENDIX

APPENDIX A: EXPLICIT EXPRESSIONS FOR $\mathcal{F}$ AND $\mathcal{G}$

In this Appendix we explicitly identify what is included in the turbulent stress terms $\mathcal{F}$ and $\mathcal{G}$ that are introduced in sections 2.1 and 3.1 and that are used throughout the paper.

We begin with the equation that expresses the conservation of momentum in a compressible, electrically conducting fluid under the magnetohydrodynamic (MHD) approximation

$$\rho\frac{\partial \mathbf{v}}{\partial t} + \rho\left(\mathbf{v}\cdot\boldsymbol{\nabla}\right)\mathbf{v} = -\boldsymbol{\nabla}P + \rho\boldsymbol{g} + \frac{1}{4\pi}\left(\boldsymbol{\nabla}\times\mathbf{B}\right)\times\mathbf{B} + \boldsymbol{\nabla}\cdot\boldsymbol{\mathcal{D}} \tag{A1}$$

Traditional notation is used: $\mathbf{v}$ is the bulk velocity of the fluid, ρ is the density, P is the pressure $\boldsymbol{g} = -g\hat{\boldsymbol{r}}$ is the

gravitational acceleration, $\mathbf{B}$ is the magnetic field, and $\boldsymbol{\mathcal{D}}$ is the viscous stress tensor, with elements

$$\mathcal{D}_{ij} = -2\rho\nu\left[e_{ij} - \frac{1}{3}\left(\boldsymbol{\nabla}\cdot\mathbf{v}\right)^2\right] \tag{A2}$$

where ν is the kinematic viscosity. We use spherical polar coordinates (r, θ, ϕ) and throughout the bulk of the paper, we consider an inertial reference frame. This lets us more gracefully incorporate the differential and uniform rotation components into a single, non-uniform rotation profile, Ω. However, for the benefit of readers, in this Appendix we wish to illustrate explicitly where the Coriolis force enters into this analysis.

Thus, we can convert equation (A1) into a rotating coordinate system (r, θ, ϕ') by writing $\mathbf{v} = \mathbf{u} + \Omega_0\lambda\hat{\boldsymbol{\phi}}$ and $\phi_r = \phi + \Omega_0 t$. Substituting these changes into (A1) yields

$$\rho\frac{\partial\mathbf{u}}{\partial t} + \rho\left(\mathbf{u}\cdot\boldsymbol{\nabla}\right)\mathbf{u} = -\boldsymbol{\nabla}P + \rho\boldsymbol{g} - 2\rho\boldsymbol{\Omega_0}\times\mathbf{u} - \rho\boldsymbol{\Omega_0}\times\left(\boldsymbol{\Omega_0}\times\boldsymbol{\lambda}\right) + \frac{1}{4\pi}\left(\boldsymbol{\nabla}\times\mathbf{B}\right)\times\mathbf{B} + \boldsymbol{\nabla}\cdot\boldsymbol{\mathcal{D}}_r \tag{A3}$$

where $\boldsymbol{\Omega_0} = \Omega_0\hat{\boldsymbol{z}}$, $\boldsymbol{\lambda} = \lambda\hat{\boldsymbol{\lambda}}$. All derivatives are with respect to the rotating coordinate system so ϕ may be formally replaced by ϕ_r in the $\boldsymbol{\nabla}$ operators. However, this is not necessary since $\partial/\partial\phi_r = \partial/\partial\phi$ for fixed r, θ, and t. The stress tensor $\boldsymbol{\mathcal{D}}_r$ is the same as $\boldsymbol{\mathcal{D}}$ with $\mathbf{v}$ replaced by $\mathbf{u}$ (and ϕ by ϕ_r).

Multiplying the zonal component of (A3) by λ and averaging over longitude (ϕ_r) yields

$$\frac{\partial}{\partial t}\left\langle\rho\lambda u_\phi\right\rangle + \left\langle\rho\mathbf{u}_m\right\rangle\cdot\boldsymbol{\nabla}\mathcal{L} = \mathcal{F} \equiv -\boldsymbol{\nabla}\cdot\left[\left\langle\rho\lambda\mathbf{u}'u'_\phi\right\rangle - \left\langle\lambda\mathbf{B}B_\phi\right\rangle - \rho\nu\lambda^2\boldsymbol{\nabla}\Omega\right] \tag{A4}$$

where $\mathcal{L} = \lambda\left(\left\langle u_\phi\right\rangle + \lambda\Omega_0\right) = \lambda\left\langle v_\phi\right\rangle = \lambda^2\Omega$. The right-hand-side is defined as the net axial torque $\mathcal{F}$. Thus, it includes the Reynolds stress (first term), the Lorentz force (second term), and the viscous diffusion (third term). The Lorentz force may be decomposed into a contirbution from mean fields $\left\langle\mathbf{B}\right\rangle\left\langle B_\phi\right\rangle$ and a Maxwell stress, $\left\langle\mathbf{B}'B'_\phi\right\rangle$. Meanwhile, the left-hand-side of (A4) includes the Coriolis force and the nonlinear advection (inertia) associated with the mean flows, $\left(\left\langle\mathbf{v}\right\rangle\cdot\boldsymbol{\nabla}\right)\left\langle\mathbf{v}\right\rangle$.

We emphasize that equation (A4) follows directly from equation (A3) with no additional assumptions [although we have used the mass continuity equation $\partial\rho/\partial t = -\boldsymbol{\nabla}\cdot(\rho\mathbf{u})$ in the derivation]. Equation (A3) in turn follows directly from (A1). The only assumption in any of this derivation is the MHD approximation that underlies equation (A1). If we make the justified assumption that $\left\langle\rho u_\phi\right\rangle \approx \left\langle\rho\right\rangle\left\langle u_\phi\right\rangle$ (as, for example, in the anelastic approximation), then the first term on the left-hand side of (A4) is just $\partial(\left\langle\rho\right\rangle\mathcal{L})/\partial t$. Furthermore, note that $\mathbf{u}_m = \mathbf{v}_m$. We thus obtain equation (1).

Now consider the meridional components of (A3). As is well known, the gravitational and centrifugal terms can be expresed in terms of a gradient $\boldsymbol{g} + \boldsymbol{\Omega_0}\times(\boldsymbol{\Omega_0}\times\boldsymbol{\lambda}) = \boldsymbol{\nabla}(\Psi_g + \lambda^2\Omega_0^2/2)$ where Ψ_g is the gravitational potential. Furthermore, we may combine the advection and Coriolis terms as follows

$$\left(\mathbf{u}\cdot\boldsymbol{\nabla}\right)\mathbf{u} + 2\boldsymbol{\Omega_0}\times\mathbf{u} = \boldsymbol{\omega}\times\mathbf{u} + \boldsymbol{\nabla}\left(\frac{u^2}{2}\right) \quad . \tag{A5}$$

where $\boldsymbol{\omega} = \boldsymbol{\nabla}\times\mathbf{u} + 2\boldsymbol{\Omega_0} = \boldsymbol{\nabla}\times\mathbf{v}$ is the vorticity relative to the inertial frame, also referred to as the absolute vorticity. We can then divide (A3) by ρ, average over longitude, and compute the zonal component of the curl to obtain

$$\frac{\partial\left\langle\omega_\phi\right\rangle}{\partial t} + \lambda\frac{\partial\Omega^2}{\partial z} = \mathcal{B} + \mathcal{G} = \frac{\boldsymbol{\nabla}\left\langle P\right\rangle\times\boldsymbol{\nabla}\left\langle\rho\right\rangle}{\left\langle\rho\right\rangle^2} + \left\langle\frac{\boldsymbol{\nabla}P\times\boldsymbol{\nabla}\rho}{\rho^2} - \frac{\boldsymbol{\nabla}\left\langle P\right\rangle\times\boldsymbol{\nabla}\left\langle\rho\right\rangle}{\left\langle\rho\right\rangle^2}\right\rangle$$
$$+ \left\{\boldsymbol{\nabla}\times\left[\left(\boldsymbol{\nabla}\times\left\langle\mathbf{u}_m\right\rangle\right)\times\left\langle\mathbf{u}_m\right\rangle\right]\right\}\cdot\hat{\boldsymbol{\phi}}$$
$$+ \left\{\boldsymbol{\nabla}\times\left\langle\left(\boldsymbol{\nabla}\times\mathbf{u}'\right)\times\mathbf{u}' + \frac{1}{4\pi\rho}\left(\boldsymbol{\nabla}\times\mathbf{B}\right)\times\mathbf{B} + \rho^{-1}\boldsymbol{\nabla}\cdot\boldsymbol{\mathcal{D}}_r\right\rangle\right\}\cdot\hat{\boldsymbol{\phi}} \quad . \tag{A6}$$

Again, this equation follows directly from equation (A3) with no further assumptions. The second term on the left-hand-side, involving Ω^2 includes the Coriolis force and the inertia associated with the differential rotation, $\left\langle u_\phi\right\rangle$. The term on the right-hand-side involving the mean meridional circulation, $\left\langle\mathbf{u}_m\right\rangle$ is estimated to be about two orders of magnitude smaller than this. Since we wish to focus on the primary components that contribute to the force balance and the inertia of the mean flow, we include the meridional circulation term with the turbulent stress term $\mathcal{G}$. Alternatively, since the kinetic energy density of the convection is at least two orders of magnitude larger than that in the meridional circulation, it is justified to neglect the meridional flow term in $\mathcal{G}$ altogether, relative to the Reynolds stress.

The first term on the right-hand-side of equation (A6) is the baroclinic term associated with the mean stratification, $\left\langle\rho\right\rangle$ and $\left\langle P\right\rangle$, which we define as $\mathcal{B}$ in equation (9). The remaining terms on the right-hand-side of equation (A6) define the turbulent stress $\mathcal{G}$. Thus, $\mathcal{G}$ includes residual baroclinic forcing involving fluctuating density and pressure components ρ' and P'. In fact, if we again make the approximation that $\rho \approx \left\langle\rho\right\rangle$ to lowest order, then this residual baroclinic term is just proportional to $\left\langle\boldsymbol{\nabla}\rho'\times\boldsymbol{\nabla}P'\right\rangle$. Other contributions to $\mathcal{G}$ include the nonlinear advection of the

mean meridional flow (the term involving $\langle \mathbf{u}_m \rangle$, which is likely negligible as noted above), the Reynolds stress (the term involving $\mathbf{u}'$), the Lorentz force (the term involving $\mathbf{B}$), and the viscous diffusion (the term involving $\boldsymbol{\mathcal{D}}$).

We use the term *turbulent stresses* loosely, since it is clear that $\mathcal{F}$ and $\mathcal{G}$ may in principle include contributions from the large-scale Lorentz force and the viscous diffusion, which need not be turbulent. However, these are not likely to be important in the solar NSSL. The small molecular viscosity of the solar plasma makes viscous diffusion negligible and the persistence of the NSSL throughout the solar cycle suggests that it is not maintained by the large-scale Lorentz force. Thus, we expect that the dominant components of $\mathcal{F}$ and $\mathcal{G}$ are indeed the turbulent Reynolds and Maxwell stresses associated with small-scale convection.

APPENDIX B: AN ANALYTIC ILLUSTRATION OF GYROSCOPIC PUMPING

Because it is essentially non-local and thus sensitive to the global geometry, boundary conditions, and inhomogeneities, gyroscopic pumping is a subtle phenomenon that generally requires numerical calculations to find equilibrium states. Still, analytic solutions can be found for idealized cases. Here we present such an analytic solution in the context of the solar NSSL. For others, see Haynes et al. (1991), Garaud & Brummell (2008), Garaud & Arreguin (2009), and Garaud & Bodenheimer (2010).

We emphasize again the point made in §2.1; that the gyroscopic pumping equation (2) can induce a meridional flow with relatively little impact on the rotational shear. Here we illustrate this by independently specifying both a differential rotation profile $\Omega(\lambda)$ and a zonal force $\mathcal{F}$ and then proceeding to derive a solution for the meridional flow that links the two.

We restrict our attention to the northern hemisphere. Solutions for the southern hemisphere then follow by symmetry. Consider a simple, cylindrical angular velocity profile given by

$$\Omega = \Omega_0 + \Delta\Omega \frac{\lambda}{R} \quad . \tag{B1}$$

This, by construction, satisfies the steady state $(\partial \langle \omega_\phi \rangle / \partial t = 0)$ meridional force balance (eq. (8)) with $\mathcal{B} = \mathcal{G} = 0$. In this appendix we will find a steady solution $\Psi(\lambda, z)$ to the zonal force balance equation (2) for the Ω profile in (B1) and a specified torque $\mathcal{F}$. We will treat the differential rotation $\Delta\Omega$ as a free parameter. Note that this is not a unique solution in the sense that other mean flow profiles $\Omega(\lambda)$, $\Psi(\lambda, z)$ can be realized with the same $\mathcal{F}$. The equilibrium solution that will be realized in practice will depend on the initial and boundary conditions of the full time-dependent system.

Here we consider a zonal torque of the form

$$\mathcal{F} = \mathcal{F}_0(r^2 + ar + b)r \sin^2\theta \cos^2\theta \qquad \text{(Region 1: } r_s \leq r \leq R) \tag{B2}$$

$$= \qquad\qquad 0 \qquad\qquad\qquad \text{(Region 2: } r < r_s, z \geq z_e) \tag{B3}$$

$$= \qquad\qquad \mathcal{F}_e(r, \theta) \qquad\qquad \text{(Region 3: } z < z_e) \tag{B4}$$

where $\mathcal{F}_0$ is the amplitude of the force and r_s is the bottom of the NSSL (Region 1). The coefficients a and b will be chosen to ensure that the meridional flow is continuous across r_s. Also, we'll choose a, b, and $\mathcal{F}_0$ to give us a negative $\mathcal{F}$ in Region 1. The latitudinal dependence in (B2) is chosen to produce a v_θ that peaks at mid-latitudes, going as $\sin\theta\cos\theta$ in the limit $\Delta\Omega \to 0$ (see eq. (B18) below). The boundary layer at the equator (Region 3, equation (B4)] is included to close the circulation cell in the northern hemisphere and to ensure that the net torque $\int_V \mathcal{F}dV = 0$. Since is it a passive response, we will compute it only after we have computed the mean flow in Regions 1 and 2. The free parameters that specify $\mathcal{F}$ are thus the amplitude in the NSSL, $\mathcal{F}_0$, and the locations of the boundary layers, r_s and z_e.

From equation (B1) we have

$$\frac{d\mathcal{L}}{d\lambda} = 2\Omega_0\lambda\left(1 + \gamma\lambda\right) \tag{B5}$$

where $\gamma = 3\Delta\Omega/(2\Omega_0 R)$.

Equation (2) yields the $\hat{\boldsymbol{\lambda}}$ component of the flow in Region 1:

$$\langle \rho v_\lambda \rangle = \beta \, \frac{r^2 + ar + b}{1 + \gamma\lambda} \, \frac{\lambda z^2}{r^3} \qquad \text{(Region 1)} \tag{B6}$$

where $\beta = \mathcal{F}_0/(2\Omega_0)$. In obtaining (B6) we have used the relations $\lambda = r\sin\theta$ and $z = r\cos\theta$.

Equation (6) then yields

$$\Psi(\lambda, z') = \tfrac{\beta\lambda}{1+\gamma\lambda}\left[I(\lambda, z) - I(\lambda, z_b)\right] \qquad (z_s \leq z' \leq z_b) \tag{B7}$$

$$\Psi(\lambda, z') = \qquad \Psi(\lambda, z_s) \qquad\qquad (z_e \leq z' < z_s)$$

$$\Psi(\lambda, z') = \qquad \Psi_3(\lambda, z) \qquad\qquad (0 \leq z' < z_e)$$

where $z_b = \sqrt{R^2 - \lambda^2}$ as in §2, $z_s = \sqrt{r_s^2 - \lambda^2}$, and we will specify $\Psi_3(\lambda, z)$ below. The solution in Region 1 involves
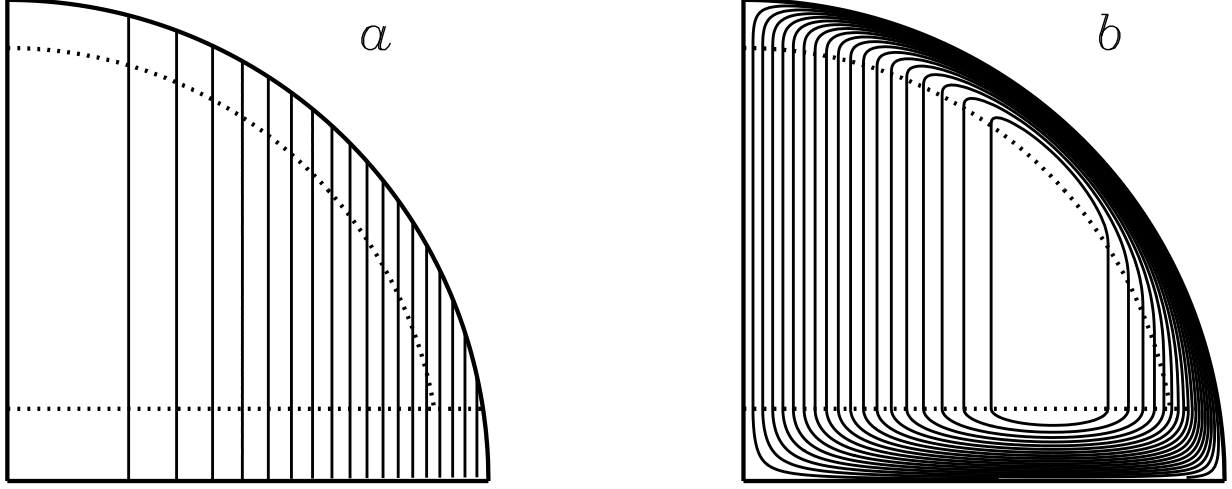
Fig. 11.— The analytic solution for (a) $\mathcal{L}$ and (b) Ψ according to equations (B1) and (B7). Here the NSSL is a bit wide, $r_s = 0.90R$ (indicated by the dotted line), in order to highlight the structure of the boundary layer. Here we've taken $\gamma = 0.45R^{-1}$ and $z_e = 0.15R$. Contours in (b) represent streamlines of the mass flux, with poleward flow at the surface. Dotted lines delineate Regions 1, 2, and 3.

the following integral

$$I(\lambda, z) = \int \left(r^2 + ar + b \right) \frac{z^2}{r^3} \, dz = \frac{z}{2r} \left(r^2 + 2ar - 2b \right) + \left(b - \frac{\lambda^2}{2} \right) \ln |z + r| - a\lambda \tan^{-1} \left(\frac{z}{\lambda} \right) \quad . \tag{B8}$$

We have dropped the integration constant because we'll use this as a definite integral in what follows.

In order to compute the coefficients a and b we will need the axial flow component, which follows from equation (5)

$$\langle \rho v_z \rangle = -\beta \, \frac{2 + \gamma\lambda}{(1 + \gamma\lambda)^2} \left[I(\lambda, z) - I(\lambda, z_b) \right] - \frac{\beta\lambda}{1 + \gamma\lambda} \left[\frac{\partial}{\partial\lambda} I(\lambda, z) - \frac{\partial}{\partial\lambda} I(\lambda, z_b) \right] \qquad \text{(Region 1)} , \tag{B9}$$

with $\langle \rho v_z \rangle = \langle \rho v_z \rangle |_{z = z_s}$ in Region 2.

Note that the term in equation (B9) involving $I(\lambda, z) - I(\lambda, z_b)$ vanishes at $z = z_b$ but as we'll see below, the term involving their derivatives does not. This is consistent with the impenetrable boundary condition $v_r = 0$ at $r = R$ since the nonzero v_θ has both v_λ and v_z components.

The derivatives in equation (B9) are given by

$$\frac{\partial}{\partial\lambda} I(\lambda, z) = \left(r^2 + 2ar + 2b \right) \frac{\lambda z}{2r^3} - \lambda \ln |z + r| + \frac{2b - \lambda^2}{z + r} \, \frac{\lambda}{2r} - a \tan^{-1} \left(\frac{z}{\lambda} \right) \tag{B10}$$

and

$$\frac{d}{d\lambda} I(\lambda, z_b) = \left(2b - R^2 \right) \frac{\lambda}{2Rz_b} - \lambda \ln |z_b + R| - \frac{2b - \lambda^2}{z_b + R} \, \frac{\lambda}{2z_b} - a \tan^{-1} \left(\frac{z_b}{\lambda} \right) \quad , \tag{B11}$$

where we have used $dz_b/d\lambda = -\lambda/z_b$.

Now we proceed to compute the coefficients a and b. Since $v_\lambda = 0$ for $r < r_s$, then continuity of v_λ requires that it should vanish at $r = r_s$ as well, along with the forcing $\mathcal{F}$. Using (B2), this can be achieved if $b = -r_s (r_s + a)$.

As a consequence of the way we set up the problem, we also have

$$\frac{\partial}{\partial\lambda} \left(\lambda \rho v_\lambda \right) = \frac{\partial}{\partial z} \left(\rho v_z \right) = 0 \qquad \text{(Region 2)} \quad . \tag{B12}$$

So, in order for the circulation to be continuous, we require these expressions to hold at $r = r_s$ as well. It is straightforward to show from equation (B6) that equation (B12) is satisfied at $r = r_s$ if $r_s^2 + 2ar_s + 3b = 0$. Combining this with the previous expression then yields $a = -2r_s$ and $b = r_s^2$.

Note that with these values of a and b, we have $r^2 + ar + b = (r - r_s)^2$. So, if we choose a negative value for $\mathcal{F}_0$ (which implies $\beta < 0$), then equation (B2) ensures that $\mathcal{F} < 0$ in the NSSL, as desired.

This completes the solution for $\Psi(\lambda, z)$ in Regions 1 and 2. For Region 3 we can then set

$$\Psi_3(\lambda, z) = \frac{z}{z_e^2} \left(2z_e - z \right) \, \Psi(\lambda, z_e) + \frac{z}{z_e} \left(z - z_e \right) \Psi'(\lambda, z_e) \quad , \tag{B13}$$

where $\Psi' = \partial\Psi/\partial z = \langle \rho v_\lambda \rangle$. The value at $z = z_e$ is zero for $r_e < r_s$ and is given by equation (B6) for $r_e > r_s$. Here $r_e = (z_e^2 + \lambda^2)^{1/2}$. It is straightforward to show that this yields $\Psi = 0$ at $z = 0$, implying no flow across the equatorial

plane, and furthermore, that Ψ, $\partial\Psi/\partial\lambda$, and $\partial\Psi/\partial z$ are continuous across $z = z_e$. The analytic solution is plotted in Figure 11.

The corresponding cylindrically outward flow in Region 3 is given by equation (5)

$$\langle\rho v_\lambda\rangle = \frac{2}{z_e^2}(z_e - z)\,\Psi(\lambda, z_e) + \frac{2z - z_e}{z_e}\Psi'(\lambda, z_e) \qquad \text{(Region 3)} \quad, \tag{B14}$$

while equation (2) gives the required torque

$$\mathcal{F}_3(\lambda, z) = \frac{d\mathcal{L}}{d\lambda}\langle\rho v_\lambda\rangle \tag{B15}$$

with $d\mathcal{L}/d\lambda$ given by (B5) and $\langle\rho v_\lambda\rangle$ given by (B14). Note that the volume-integrated torque is zero by construction, as a consequence of the impenetrable boundaries and equation (2)

$$\int_V \mathcal{F}\,dV = \int_V \langle\rho\mathbf{v}_m\rangle\cdot\boldsymbol\nabla\mathcal{L}\,dV = \int_S \boldsymbol\nabla\cdot(\langle\rho\mathbf{v}_m\rangle\,\mathcal{L})\cdot d\mathbf{S} = 0 \quad. \tag{B16}$$

The axial flow in Region 3 follows from equations (5), (B9), and (B13)

$$\langle\rho v_z\rangle = \qquad\qquad \frac{z}{z_e^2}(2z_e - z)\,\langle\rho v_z\rangle|_{z=z_s} \qquad\qquad \text{(Region 3, } r \leq r_s)$$

$$\langle\rho v_z\rangle = \frac{z}{z_e^2}(2z_e - z)\,\langle\rho v_z\rangle|_{z=z_e} - \beta\frac{z^3\lambda}{r^3 z_e}\frac{(r-r_s)^2}{1+\gamma\lambda}(z - z_e)\left(\frac{2}{r-r_s} + \frac{2}{\lambda} - \frac{\gamma}{1+\gamma\lambda} - \frac{3\lambda}{r^2}\right) \qquad \text{(Region 3, } r > r_s) \quad.$$

It is instructive to verify that the flow at the outer boundary is indeed poleward. Substituting $z = z_b$ and $r = R$ into equations (B6) and (B9) and expressing the result in spherical coordinates yields

$$\langle\rho v_\lambda\rangle = \frac{\beta D^2}{1 + \gamma R\sin\theta}\,\sin\theta\cos^2\theta \quad, \text{ and } \quad \langle\rho v_z\rangle = -\frac{\beta D^2}{1 + \gamma R\sin\theta}\,\sin^2\theta\cos\theta \quad (r = R) \tag{B17}$$

where $D = R - r_s$ is the thickness of the NSSL. Furthermore,

$$\langle\rho v_\theta\rangle = -\sin\theta\,\langle\rho v_z\rangle + \cos\theta\,\langle\rho v_\lambda\rangle = \frac{\mathcal{F}_0 D^2}{2\Omega_0}\,\frac{\sin\theta\cos\theta}{1 + (\Delta\Omega/\Omega_0)\sin\theta} \qquad (r = R) \quad, \tag{B18}$$

and $\langle\rho v_r\rangle = \cos\theta\,\langle\rho v_z\rangle + \sin\theta\,\langle\rho v_\lambda\rangle = 0$ at $r = R$. For $\mathcal{F}_0 < 0$, equation (B18) implies a poleward flow.

This is clearly a highly idealized depiction of a star. In the solar convective envelope, strong turbulent stresses $\mathcal{F}$ (and possibly $\mathcal{G}$) and baroclinic forcing $\mathcal{B}$ maintain a substantial non-cylindrical differential rotation profile (Fig. 1) and this will in turn determine how the meridional circulation streamlines close in Regions 2 and 3. In particular, the initial circulations established by convection on a dynamical time scale are unlikely to penetrate much below the convection zone (Gilman & Miesch 2004), although very weak gyroscopically-pumped circulations driven by convection will burrow downward on a radiative diffusion time scale, eventually reaching the deep radiative interior over the course of billions of years (Spiegel & Zahn 1992; Gough & McIntyre 1998; Garaud & Brummell 2008). Here turbulent stresses are weak $\mathcal{F} \approx 0$ and the rotation is nearly uniform so the circulation contours would follow cylindrical surfaces as in Region 2 of the present example. In any case, the solution discussed in this section is only intended to give a rough feel for how gyroscopic pumping in the NSSL might impact the dynamics in the upper convection zone.

Still, equations (B1), (B7), (B8), and (B13). provide a steady, analytic solution to the continuity, momentum, and energy equations in the barotropic (or isentropic) limit $(P = P(\rho))$ under the influence of specified turbulent stresses analogous to the NSSL ($\mathcal{F} < 0$ for $r > 0.95$). They also highlight the need for turbulent or baroclinic stresses in the meridional plane, $\mathcal{B}$ and/or $\mathcal{G}$, in order to maintain an axial rotational shear $\partial\Omega/\partial z \neq 0$.

APPENDIX C: UNCURLING THE ZONAL VORTICITY EQUATION

As described in §4.3, we wish to derive the acceleration $\mathbf{A}_m$ corresponding to the meridional stress $\mathcal{G}$. To do this, we must solve equation (23) for ζ. The expansion for Ω in equation (16) implies that we can write ζ as

$$\zeta(r, \theta) = \sin\theta\sum_n Z_n(r)\cos^n\theta \qquad (n = 1, 3, 5, 7, 9). \tag{C1}$$

Each of the $Z_n(r)$ satisfy a recursive equation of the form

$$Z_n'' + \frac{2}{r}Z_n' - \frac{1}{r^2}\left(n^2 + 3n + 2\right)Z_n = -\Gamma_n - \frac{1}{r^2}(n+1)(n+2)Z_{n+2} \tag{C2}$$

where primes denote (ordinary) derivatives with respect to r and $Z_n = 0$ for n even and for $n > 9$. The Γ_n are given by

$$\Gamma_1 = -2r\Omega_e d_1 \quad \Gamma_3 = -2r\left(\Omega_e d_3 + \Omega_2 d_1\right) \quad \Gamma_5 = -2r\left(\Omega_e d_5 + \Omega_2 d_3 + \Omega_4 d_1\right) \tag{C3}$$

$$\Gamma_7 = -2r\left(\Omega_2 d_5 + \Omega_4 d_3\right) \qquad\qquad \Gamma_9 = -2r\Omega_4 d_5 \tag{C4}$$

where

$$d_1 = \Omega'_e + \frac{2}{r}\Omega_2 \qquad d_3 = \Omega'_2 - \frac{2}{r}\Omega_2 + \frac{4}{r}\Omega_4 \qquad d_5 = \Omega'_4 + \frac{2}{r}\Omega_2 - \frac{4}{r}\Omega_4 \quad . \tag{C5}$$

The radial derivatives in equations (C2) and (C5) are discretized using a second-order finite difference scheme and the resulting matrix equations are solved subject to the boundary conditions $Z_n = 0$ at $r = R$ and $rZ'_n + Z_n = 0$ at $r = r_s$. These boundary conditions ensure that the vertical acceleration vanishes at the surface ($A_r = 0$ at $r = R$) and the horizontal acceleration vanishes at the base of the NSSL ($A_\theta = 0$ at $r = r_s$).

APPENDIX D: DIFFUSIVE ANGULAR VELOCITY PROFILES

In this Appendix we seek angular velocity profiles for which the net axial torque vanishes $\mathcal{F} = 0$, subject to the boundary conditions

$$\Omega(r_s, \theta) = \hat{\Omega}_0 + \hat{\Omega}_2 \cos^2 \theta + \hat{\Omega}_4 \cos^4 \theta = \omega_0 + \omega_2 P_2(\cos \theta) + \omega_4 P_4(\cos \theta) \tag{D1}$$

and

$$\left.\frac{\partial \Omega}{\partial r}\right|_{r=r_s} = 0 \tag{D2}$$

at a specified matching layer, $r = r_s$. Here $\hat{\Omega}_0$, $\hat{\Omega}_2$ and $\hat{\Omega}_4$ are fitting coefficients corresponding to the solar rotation profile at the matching layer ($r = r_s$), as inferred from global helioseismology (Fig. 1). The expression on the far right of equation (D1) provides an alternate representation of $\Omega(r_s, \theta)$ in terms of Legendre Polynomials $P_n(x)$. The Legendre coefficients are given by

$$\omega_0 = \hat{\Omega}_0 + \frac{\hat{\Omega}_2}{3} + \frac{\hat{\Omega}_4}{5} \qquad \omega_2 = \frac{2}{3}\hat{\Omega}_2 + \frac{4}{7}\hat{\Omega}_4 \qquad \omega_4 = \frac{8}{35}\hat{\Omega}_4 \quad . \tag{D3}$$

We choose r_s to correspond to the location where the radial gradient of the spherically-averaged angular velocity profile passes through zero. This yields values of $r_s = 0.946R$, $\hat{\Omega}_0/(2\pi) = 468$ nHz, $\hat{\Omega}_2/(2\pi) = -62.5$ nHz, and $\hat{\Omega}_4/(2\pi) = -77.9$ nHz.

We consider two hypothetical forms for $\mathcal{F}$, representing turbulent diffusion and the mixing of angular momentum as discussed in §5. In the first case the angular momentum flux is given by equation (28). The assumption of no net torque and a constant density-weighted diffusion coefficient $\rho\nu_t$ then yields equation (31): $\boldsymbol{\nabla}(\lambda^2 \boldsymbol{\nabla}\Omega_v) = 0$. The solution can be written as a Legendre series

$$\Omega_v(r, \theta) = W_0(r) + W_2(r)P_2(\cos \theta) + W_4(r)P_4(\cos \theta) \tag{D4}$$

with coefficients

$$W_4(r) = a_1\left(r^4 + a_2 r^{-7}\right) \tag{D5}$$

$$W_2(r) = b_1 r^4 + b_2 r^{-7} + b_3 r^2 + b_4 r^{-5} \tag{D6}$$

$$W_0(r) = c_1 r^4 + c_2 r^{-7} + c_3 r^2 + c_4 r^{-5} + c_5 r^{-3} + c_6 \tag{D7}$$

where

$$a_2 = \frac{4}{7}r_m^{11} \qquad a_1 = \frac{\omega_4}{r_m^4 + a_2 r_m^{-7}} \qquad b_1 = \frac{5}{9}a_1 \qquad b_2 = \frac{5}{9}a_1 a_2 \tag{D8}$$

$$b_3 = \frac{5}{7}\omega_2 r_m^{-2} - \frac{9}{7}b_1 r_m^2 + \frac{2}{7}b_2 r_m^{-9} \qquad\qquad b_4 = \omega_2 r_m^5 - b_1 r_m^9 - b_2 r_m^{-2} - b_3 r_m^7 \tag{D9}$$

$$c_1 = \frac{a_1 + b_1}{14} \qquad c_2 = \frac{a_1 a_2 + b_2}{14} \qquad c_3 = \frac{b_3}{5} \qquad c_4 = \frac{b_4}{5} \tag{D10}$$

$$c_5 = \frac{1}{3}\left(4c_1 r_m^7 - 7c_2 r_m^{-4} + 2c_3 r_m^5 - 5c_4 r_m^{-2}\right) \qquad c_6 = \omega_0 - c_1 r_m^4 - c_2 r_m^{-7} - c_3 r_m^2 - c_4 r_m^{-5} - c_5 r_m^{-3} \quad . \tag{D11}$$

For the second case we consider, that of angular momentum mixing, the angular momentum flux is given by equation (29) and the rotation profile for $\mathcal{F} = 0$ and $\rho\nu_a = $ constant is given by equation (32), $\nabla^2 \mathcal{L}_a = 0$. The solution is readily obtained through a Legendre series

$$\mathcal{L}_a(r, \theta) = \sum_n \frac{r^n + \beta_n r^{-(n+1)}}{r_m^n + \beta_n r_m^{-(n+1)}} L_n P_n(\cos \theta) \qquad (n = 0, 2, 4, 6). \tag{D12}$$

Here L_n are the coefficients corresponding to the matching layer

$$L_6 = -\frac{16}{231}\hat{\Omega}_4 r_m^2 \qquad\qquad L_4 = \frac{8}{35}\left(\hat{\Omega}_4 - \hat{\Omega}_2\right)r_m^2 + \frac{9}{2}L_6 \tag{D13}$$

$$L_2 = \frac{2}{3}\left(\hat{\Omega}_2 - \hat{\Omega}_0\right)r_m^2 + \frac{5}{2}L_4 - \frac{35}{8}L_6 \qquad\qquad L_0 = \hat{\Omega}_0 r_m^2 + \frac{L_2}{2} - \frac{3}{8}L_4 + \frac{5}{16}L_6 \qquad\qquad \text{(D14)}$$

and $\beta_n = [(n-2)/(n+3)]\ r_m^{2n+1}$. The corresponding rotation profile is then $\Omega_a = \lambda^{-2}\mathcal{L}_a$.
The two solutions derived here, $\Omega_v(r,\theta)$ and $\Omega_a(r,\theta)$ are shown in Figure 9.